Journal of Alloys and Compounds 1044 (2025) 184299

Contents lists available at ScienceDirect

Journal of Alloys and Compounds

journal homepage: www.elsevier.com/locate/jalcom

Impacts of the electronic structures of group IB element-centered single-atom nanozymes on their catalytic activities and management of peri-implantitis

Yuqing Liu [a,b,1], Ting Ma [c,1], Ye Feng [d], Zhaoyu Li [d], Lei Yan [b], Huaiyu Wang [b,*], Dongdong Zhang [b,e,*], Paul K. Chu [e], Donghui Wang [d,**]

[a] School of Advanced Manufacturing, Fuzhou University, 1 Shuicheng Road, Jinjiang, Fujian 362251, PR China
[b] Center for AI-Driven Medical Research, Shenzhen Institute of Advanced Technology, Chinese Academy of Sciences, Shenzhen 518055, China
[c] Department of Oral Implantology, Peking University School and Hospital of Stomatology, 22 Zhongguancun South Avenue, Haidian District, Beijing 10081, PR China
[d] Hebei Key Laboratory of Biomaterials and Smart Theranostics, School of Health Sciences and Biomedical Engineering, Hebei University of Technology, Tianjin 300130, China
[e] Department of Physics, Department of Materials Science & Engineering, and Department of Biomedical Engineering, City University of Hong Kong, Tat Chee Avenue, Kowloon, Hong Kong, China

ARTICLE INFO

Keywords:
Single-atom nanozymes
Peroxidase-like catalytic activity
Photothermal
Anti-bacterial
Osteogenesis

ABSTRACT

Carbon-supported metal-containing single-atom nanozymes (SAEs) with bioinspired M1−N4 structures exhibit catalytic activity and photothermal properties that are important for combating implant-associated infections. However, how the electronic structures of M1−N4 sites influence the enzymatic activity is not well-understood. In this study, three uniform M1−N4/C (M = Cu, Ag, or Au) SAEs were synthesized to investigate the effects of the *d*-band electronic structure of each metal atom on the catalytic activity, associated physicochemical properties, and antibacterial applications of the nanozyme. Experimental investigations and theoretical calculations revealed an inverse correlation between the •OH-induced oxidation activity and *d*-band electronic layer. Additionally, Cu-SAE exhibited the most pronounced peroxidase-like activity and glutathione consumption capacity. Moreover, the three SAEs exhibited excellent photothermal conversion activities. *In vitro* experiments demonstrated that all three nanozymes exhibited robust bactericidal effects against *Escherichia coli*, *Staphylococcus aureus*, and *Streptococcus mutans* under catalytic and near-infrared (NIR) light-stimulated conditions, with Cu-SAE showing the most potent activity. Moreover, they all maintained excellent cell safety profiles. In animal studies, 0.5 % H_2O_2 with Cu-SAE exhibited superior antibacterial efficacy, biocompatibility, and osseointegration capability compared with a traditional decontaminant (3 % H_2O_2) under controlled NIR light-triggered conditions.

1. Introduction

Owing to population aging and increased healthcare awareness, incidences of dental diseases are on the rise globally, and the demand for implants continues to grow. Titanium (Ti) implants lack antimicrobial activity and osseointegration capability; hence, they are unsuitable for current clinical use [1–3]. The formation of complex plaque biofilms on Ti-based implants renders the devices susceptible to attack by pathogenic bacteria, which increases the risk of peri-implant inflammation [4–7]. As the primary clinical treatment for bacterial infections, antibiotic therapies seem to be trapped in a vicious cycle because bacteria can develop resistance to a new drug within a few years of its clinical application [8,9]. Commercially available biofilm removers (e.g., 3 % hydrogen peroxide (H_2O_2)) are not clinically effective in removing plaque biofilms from implant surfaces. Moreover, high concentrations of H_2O_2 may irritate gingival tissue and damage the implant

* Corresponding authors.
** Corresponding author at: Center for AI-Driven Medical Research, Shenzhen Institute of Advanced Technology, Chinese Academy of Sciences, Shenzhen 518055, China.
E-mail addresses: hy.wang1@siat.ac.cn (H. Wang), dd.zhang2@siat.ac.cn (D. Zhang), donghuiwang@hebut.edu.cn (D. Wang).
[1] These authors contributed equally to this work

https://doi.org/10.1016/j.jallcom.2025.184299
Received 31 July 2025; Received in revised form 29 September 2025; Accepted 8 October 2025
Available online 10 October 2025

[10], thereby inhibiting normal tissue cell proliferation and osteogenic differentiation [11–13]. Therefore, the effective and safe removal of plaque biofilms from implants is an urgent, but challenging, clinical issue.

Enzymes are natural catalysts that reduce the activation energy and increase the rate of chemical reactions [14–16]. Nanozymes exhibit high catalytic stability and environmental tolerance and are suitable for large-scale production and storage. As synthetic substances, nanozymes also carry the advantages of having adjustable active sites and being easily functionalized [17–19], and they can protect against exogenous microbial invasion and ensure optimal wound conditions for accelerated healing [20]. In particular, single-atom nanozymes (SAEs) with well-defined structures, catalytic site coordination, and high atom utilization efficiency are highly promising and effective catalysts [21,22]. Among these, metal–nitrogen–carbon (MNC) SAEs have attracted considerable interest as their M–N*x* structures are similar to that of natural horseradish peroxidase [8], [23]. M1–N4 SAEs can donate electrons to the peroxide group to generate large amounts of reactive oxygen species (ROS), leading to excellent photothermal conversion and biofilm-scavenging properties [24]. The catalytic activity and photothermal conversion efficiency of many SAEs can be optimized by changing the specific surface area of the carbon carriers and the type of doped element for the metal centers [25,26]. Although the composition of SAEs is the key factor determining their effects, the influences of their metal atomic centers are not well-understood. Moreover, the relationship between the electronic structure of the metal and the catalytic properties of the SAE needs to be clarified to facilitate better designing of multiphase catalysts. Recent studies of SAEs have shown that the presence of more outer electrons in the core of metal atoms with the same number of electron layers outside the nucleus can enhance bonding with the substrate, optimize electron transfer, and promote more efficient reactions [27]. Simultaneously, an abundance of outer electrons can confer unique properties to the active sites and enhance the recognition and binding of the substrate [28]. Research by Wang Ying et al. demonstrates that reducing the electron density at the Fe center enhances the adsorption energy of oxygen species, thereby significantly improving its enzyme-like catalytic efficiency. By utilizing heteroatom coordination to regulate the electronic spin state and valence state of the Mn center, the material's multiple enzymatic activities (oxidase, peroxidase, and superoxide dismutase (SOD)) can be modulated [29,30]. Furthermore, researchers have constructed copper-based SAEs with SOD-like activity by mimicking the electronic structure of natural enzyme metal sites, achieving highly specific catalysis of superoxide anion dismutation reactions. This demonstrates the determining role of metal electronic structures in enzyme-like specificity and activity [31]. However, the influence of the number of extranuclear electron layers on the catalytic activity of SAEs containing metals with the same number of outermost electrons at the atomic core has not been investigated. Group IB elements belong to the same main group, with the number of valence electron shells progressively increasing. This leads to a corresponding increase in the energy difference between d and s orbitals. This gradient variation in electron shells facilitates the analysis of how the number of valence electron shells affects SAEs [32,33]. Furthermore, certain Group IB elements such as copper (Cu), silver (Ag), and gold (Au) inherently possess antimicrobial properties. These properties can synergize with the catalytic activity of SAEs and thus facilitate the antimicrobial effects [34,35]. It is important to explore the influences of Group IB elements, such as copper (Cu), silver (Ag), and gold (Au), which have some antimicrobial effects [36,37]. used as metal centers of SAEs on the catalytic activities, photothermal conversion properties, and antimicrobial applications of the nanozyme.

Therefore, in this study, Cu, Ag, and Au were used as metal centers to prepare M-SAEs (Cu-SAE, Ag-SAE, and Au-SAE, respectively) for determining the effects of the number of electron layers of metal atoms on the catalytic activity, physicochemical properties, and applications of the nanozyme. The peroxidase (POD)-like activity and mechanisms were evaluated on the basis of experimental results and theoretical calculations. The three M-SAEs prepared in this study showed robust glutathione peroxidase-like activities and photothermal conversion abilities. Additionally, their antimicrobial performances against *Escherichia coli*, *Staphylococcus aureus*, and *Streptococcus mutans* were assessed, with a focus on their abilities to scavenge *S. mutans* biofilms. Animal experiments were conducted to compare Ti implants treated with Cu-SAE with those treated with 3 % H_2O_2 in terms of their bactericidal effects and capacities to promote pericyte proliferation and osteogenic differentiation.

2. Experimental section

2.1. Materials and reagents

Zinc nitrate hexahydrate ($Zn(NO_3)_2{\cdot}6\ H_2O$), 2-methylimidazole, copper nitrate trihydrate ($Cu(NO_3)_2{\cdot}3\ H_2O$), silver nitrate ($AgNO_3$), chloroauric acid tetrahydrate ($HAuCl_4{\cdot}4\ H_2O$), sodium dicyandiamide (DCDA), melamine (MA), hydrogen peroxide (H_2O_2, 30 wt%),3,3',5,5'-Tetramethylbenzidine (TMB), O-phenylenediamine (OPDA), glutathione (GSH) and 5, 5′-dithio-bis (2-nitrobenzoic acid) (DTNB) were purchased from Aladdin Chemical Reagent Co., Ltd.

2.2. Synthesis of M-doped single-atom nanozyme (M-SAE)

2.2.1. Synthesis of ZIF-8

The ZIF-8 precursors were prepared by adding 2.65 g of Zn (NO3)2·6H2O to 40 mL of methanol to form solution A and adding 2-methylimidazole (8 g) to 120 mL of methanol to obtain solution B. Solutions A and B were mixed vigorously for 1 h and then allowed to stand at 25 °C for 24 h. The product was centrifuged, washed with methanol and ethanol three times, and dried in a vacuum drying oven to obtain the ZIF-8 precursor.

2.2.2. Preparation of NPC-900

The ZIF-8 precursor powder was heated to 900 ° C at a heating rate of 5 ℃ min^{-1} and kept at 900 ° C for 2 h under flowing Ar in a tube furnace. After cooling to room temperature, the product was processed with 1 M H_2SO_4 at 80 ℃ for 8 h, filtered, washed several times with deionized water and ethanol until a neutral pH, and dried to obtain NPC-900.

2.2.3. Preparation of M-SAE

The synthesis of Cu-SAE, Ag-SAE, and Au-SAE is similar. NPC-900 (200 mg) was dispersed ultrasonically in a mixture containing 40 mL of isopropanol and 20 mL of water for 2 h to form dispersion liquid A. 200 mg of $Cu(NO3)_2{\cdot}3H2O$, 140 mg of $AgNO_3$, or 300 mg of $HAuCl_4{\cdot}4\ H_2O$, along with 0.5 g DCDA and 0.5 g MA, were dispersed in a mixture of 40 mL isopropanol and 20 mL water and sonicated for 2 h to form dispersion B. Dispersion B was added to dispersion liquid A under magnetic stirring. After 12 h, the product was obtained by centrifugation and drying. Subsequently, the precursor was then placed on a covered porcelain boat, heated to 650 ℃ at a heating rate of 2 ℃/min under Ar, and kept for 2 h to obtain the corresponding metal-doped single-atom nanozyme (M-SAE). The M-SAE samples were stirred in the appropriate acids (1 M hydrochloric acid for Cu-SAE, 2 M nitric acid for Ag-SAE, and aqua regia for Au-SAE) to remove metal particles from the surface. At the end of the acid wash, the samples were collected by filtration and washed several times with ethanol and deionized water until neutral. The M-SAE samples were labeled Cu-SAE, Ag-SAE, and Au-SAE, respectively.

2.3. Characterization

2.3.1. Materials characterization

The morphology of the M-SAE was examined by transmission electron microscopy (TEM, JEM-2100) and spherical aberration-corrected

transmission electron microscopy (AC-STEM, JEM-ARM300, Japan). X-ray diffractometer (XRD, D8 Discover, German) was conducted on the Bruker D8 Advance diffractometer equipped with a focusing Göbel mirror producing Cu Kα radiation (λCu = 1.5418 Å) and a LynxEye detector in the transmission mode. The diffraction patterns were recorded in the 2θ range of 5°-80°. X-ray photoelectron spectroscopy (XPS, ESCALAB 250Xi, America) was performed using Mg Kα as the excitation source, and the elemental distributions were characterized by SEM and energy-dispersive X-ray spectroscopy (EDS). Nitrogen physisorption was assessed using a surface and pore size analyzer (Micromeritics ASAP 2460, America) at liquid nitrogen temperature (77 K). The Raman spectra were collected on the Renishaw inVia Reflex spectrometer (England) equipped with a 532 nm laser excitation source. The Cu K-edge, Ag K-edge, and Au K-edge analyses were performed with Si (111) crystal monochromators at the BL11B beamlines in the Shanghai Synchrotron Radiation Facility (SSRF) (Shanghai, China). Before the analysis, the samples were pressed into thin sheets 1 cm in diameter and sealed with Kapton tape. The XAFS spectra were recorded at room temperature by a 4-channel silicon drift detector (SDD) Bruker 5040. The Cu K-edge, Ag K-edge, and Au K-edge extended X-ray absorption fine structure (EXAFS) spectra were recorded in the transmission mode. Negligible changes in the line shape and peak position of the XANES spectra were observed between two scans taken from a specific sample. The XAFS spectra of these standard samples were recorded in the transmission mode. The spectra were processed and analyzed by the Athena and Artemis software.

2.3.2. Peroxidase-like activity

TMB and OPDA were used as indicators to visualize and monitor the ·OH generation. In detail, a 1.0 mL acetate (NaAc) buffer containing the samples (100 μg/mL), TMB (0.5 mM), and H_2O_2 (100 μM) was incubated for 30 min at 25 ℃. UV–vis spectrophotometry was carried out.

2.3.3. Kinetics analysis of peroxidase-like enzymes

Kinetics experiments were conducted using samples and varying concentrations of the H_2O_2 substrate. The experimental procedure was similar to that described above, with a 1.0 mL NaAc buffer containing samples (100 μg/mL), TMB (0.5 mM), and H_2O_2 with different concentrations (0, 0.05, 0.1, 0.2, 0.5, and 1.0 mM). The reaction duration was set at 30 min. The v-[s] and 1/v-1/[s] images were then plotted using the Michaels-Menton equation in the GraphPad Prism software. The effects of pH, near-infrared light radiation, and reaction temperature on the peroxidase-like activity of the samples were investigated using TMB as a probe. The pH values ranged from 3.6 to 7.4, and the temperatures ranged from 25 to 65 ℃.

2.3.4. Glutathione-like peroxidase activity

The principle behind analyzing the consumption of GSH was that GSH could react with the DNTB probe and enhance the absorbance of DNTB in the 400–450 nm wavelength range. Briefly, DNTB was used as an indicator to observe and monitor GSH residual in real time. 1.0 mL of the phosphate (PBS) buffer containing the samples (250 μg/mL), GSH (1 mM), and DNTB (100 μM) was incubated for 0, 0.5, 1, and 2 h at 25 ℃, and then UV–vis spectra were acquired.

2.4. Photothermal analysis

To evaluate the photothermal effects of NPC-900 and M-SAE, 1.0 mL of an aqueous dispersion of the samples with a concentration of 250 μg/mL was added to a quartz cell and irradiated by an 808 nm laser (0.5 W/cm^2) for 5 min. The photothermal stability was determined based on three laser on/off cycles. The photothermal conversion efficiency was calculated by the following energy balance equation [38]:

$$\sum_i m_i C_i \frac{dT}{dt} = Q_P + Q_W + Q_L \quad , \tag{1}$$

where m_i and C_i are the mass and specific heat capacity of NPC-T solution, T is the temperature of NPC-T solution, and t is the laser irradiation time. Q_P is the heat generated by the photothermal conversion of NPC-T under laser irradiation. Q_W is the heat generated by the photothermal conversion of water under laser irradiation, and Q_L is the heat flowing from the system to the surrounding environment. Q_p is expressed by Eq. (2):

$$Q_P = I\left(1 - 10^{-A_{808}}\right)\eta, \tag{2}$$

where I is the laser power input to the system. A_{808} is the absorbance of the NPC-T at 808 nm, and η is the photothermal conversion efficiency of the NPC-T. Q_L is expressed by Eq. (3):

$$Q_L = hS\Delta T, \tag{3}$$

where h is the heat transfer coefficient, S is the area of the laser spot, $\Delta T = T - T_{surr}$, T is the real-time temperature of the system, and T_{surr} is the ambient temperature.

When the system temperature reaches equilibrium, the heat generated by the photothermal conversion is equal to the heat dissipated:

$$Q_P + Q_W = Q_L = hS\Delta T_{\max} \quad , \tag{4}$$

where $\Delta T_{\max}$ is the value of temperature change when the system is in equilibrium. According to Eqs. (2–4), the photothermal conversion efficiency can be derived by Eq. (5):

$$\eta = \frac{hS\Delta T_{\max} - Q_W}{I(1 - 10^{-A_{808}})} \quad . \tag{5}$$

The parameter hS is unknown, so θ can be introduced to find hS and θ is defined as:

$$\theta = \frac{\Delta T}{\Delta T_{\max}} \tag{6}$$

Eqs. (3) and (6) are combined with Eq. (1) to obtain Eq. (7):

$$\frac{d\theta}{dt} = \frac{hS}{\sum_i m_i C_i}\left(\frac{Q_P + Q_W}{hS\Delta T_{\max}} - \theta\right) \quad . \tag{7}$$

When the laser was turned off, the system cooled naturally. In this stage $Q_P + Q_W = 0$. Eq. (7) becomes:

$$t = -\frac{\sum_i m_i C_i}{hS}\ln\theta = -\tau_s \ln\theta, \tag{8}$$

where τ_s is the time dosage of the system and denotes the slope of the line between time t and -lnθ. Considering that the mass of NPC-T in the NPC suspension was 1 mg, which was much smaller than the mass of water (1 g), $m_P C_P$ could be neglected because the specific heat capacity of water was larger than that of NPC-T. Owing to the linear relationship between the natural cooling phase, t, and $-\ln\theta$, it is possible to determine hS:

$$hS = \frac{m_W C_W}{\tau_s} \quad . \tag{9}$$

Q_W in Eq. (5) could be determined by the warming process of laser irradiation of deionized water by the following equation:

$$Q_W = \frac{m_W C_W \Delta T_{\max,\, H_2O}}{\tau_s} \quad , \tag{10}$$

where m_W is the mass of deionized water. C_W is the specific heat capacity of deionized water. $\Delta T_{\max,\, H_2O}$ is the temperature change of laser irradiation of deionized water to reach the equilibrium of the system, and τ_s is the time usage of the system.

Therefore, the photothermal conversion efficiency of NPC-T solutions can be calculated according to Eqs. (5) and (8–10):

$$\eta = \frac{hS(\Delta T_{max} - \Delta T_{max,H_2O})}{I(1-10^{-A_{808}})} \quad (11)$$

where $hS = 0.01376$ W/°C, $\tau_s = 305.175$ s, $m = 1$ g, $C = 4.2$ J/g, $I = 1$ W/cm^2, and $A_{808} = 0.2765$.

2.5. Density-functional theory calculations

The spin-polarized density-functional theory (DFT) calculations were conducted based on the Vienna ab initio simulation package (VASP) [39,40] to study the properties of the materials. The Projector augmented wave method [40] with a cutoff energy of 450 eV accompanied by Perdew-Burke-Ernzerhof functional [41] was adopted, and the DFT-D3 method [42] was applied to correct for van der Waals interactions, respectively. One layer of the carbon (001) facet was cleaved with a vacuum layer of 20 Å, and six carbon atoms were replaced by CuN4, AgN4, and AuN4. The models were fully relaxed with the energy convergence criterion of 10^{-5} eV and the force convergence criterion of 0.02 eV/Å. The gamma point was used in the K-point mesh, and the adsorption energy (Eads) was calculated by Eq. (12):

$$E_{ads} = E_{total} - E_{substrate} - E_{adsorbate} \quad , \quad (12)$$

Where Etotal, Esubstrate, and Eadsorbate represent the energy of the adsorption structure, substrate, and adsorbate, respectively. The free energies were calculated by Eq. (13):

$$G = E_{DFT} + ZPE - TS, \quad (13)$$

Where G, EDFT, ZPE, and TS are the free energy, energy from DFT calculations, zero point energy, and entropic contributions, respectively.

2.6. In vitro cell experiments

2.6.1. Cell culture

The human bone marrow mesenchymal stem cells (hBMSCs; Stem Cell Bank, Chinese Academy of Sciences, Shanghai, China) were passaged every 3 days, and only three to six generations were passaged.

2.6.2. Hemolysis rate test

Ultrapure water was used as the positive control, while 0.9 wt% NaCl served as the negative control. Each sample (=250 μg/mL, 0.5 mL,) was mixed with 10 μL of diluted red blood cells and incubated at 37 ℃ for 2 h. The mixture was then centrifuged at 3000 rpm for 5 min, and the supernatant was collected. Absorbance was measured at 540 nm.

2.6.3. Cytotoxicity

hBMSCs and AlamarBlue were used to determine the cytotoxicity of the samples on a microplate reader. The cells were cultured on a 96-well plate with a density of 1×10^4 cells per well and maintained for 24 h for attachment. Afterward, a new culture of the medium containing the samples replaced the old one. After another 24 h, the medium containing 10 % AlamarBlue (100 μL) was added and incubated for 4 h in darkness. The fluorescence intensity was monitored by a fluorescence enzyme marker using an excitation wavelength of 560 nm and an emission wavelength of 590 nm. The cell viability was calculated by the following equation: cell viability (%) = $(F\text{-}F_{blank})/(F_0\text{-}F_{blank}) \times 100$ %, where F represents the fluorescence intensity of surviving cells after 1-day co-culturing with the samples, F_0 is the fluorescence intensity of the cells not co-cultured with the samples, and F_{blank} refers to the fluorescence intensity of the medium containing 10 % AlamarBlue.

2.6.4. Live/dead staining

The cells, after different treatments, were stained with calcein acetoxymethyl ester (Calcein-AM) and propidium iodide (PI) for 30 min and washed three times with PBS. Fluorescence microscopy was used to observe the live (green fluorescence) and dead (red fluorescence) cells.

2.6.5. Alkaline phosphatase (ALP) activity

The ALP activity of the samples was assessed qualitatively/quantitatively by ALP staining. The hBMSCs were inoculated onto the samples at a density of 1×10^4 cells per well. The cells on the samples were washed with PBS after 7 days, fixed with citrate-buffered acetone, stained with the ALP Kit (Ambion, USA), and observed under a fluorescence microscope (GX71, Olympus, Japan) in a bright environment. The total protein content in the cells was determined by the BCA Kit (Ambion, USA), and the ratio of the total ALP content detected by the ALP Kit to the total protein content was the ALP activity quantitatively expressed by the cells.

2.7. In vitro antibacterial activity

In the antibacterial investigations, Escherichia coli (*E. coli*, ATCC15597) was used as the model Gram (-) bacteria, while Staphylococcus aureus (*S. aureus*, ATCC6538) and Streptococcus mutans (*S. mutans*, ATCC35668) were the model Gram (+) bacterial cell strains. The *E. coli* and *S. aureus/S.mutans* strains were revived from frozen glycerol stocks by inoculation in Luria-Bertani (LB)/Brain Heart Infusion (BHI) medium overnight at 37 ℃ in an incubator. The population density of the bacterial cells was determined by measuring the absorbance at 600 nm. In a typical antibacterial assay, *E. coli*, *S. aureus*, and *S. mutans* were divided into following eight groups: (1) bacteria; (2) bacteria + NIR light; (3) bacteria + H_2O_2; (4) bacteria + NIR light + H_2O_2; (5) bacteria + samples; (6) bacteria + samples + NIR; (7) bacteria + samples + H_2O_2; (8) bacteria + samples + NIR light + H_2O_2. Groups (2), (4), (6), and (8) were further exposed to a NIR laser (808 nm, 0.5 W/cm^2) for 5 min. After NIR irradiation, the procedure was the same as that of groups (1), (3), (5), and (7). The final concentrations of samples, H_2O_2, and bacteria were 250 μg·mL^{-1}, 1 mM, and 1×10^6 CFU·mL^{-1}, respectively. After incubation for 15 min, 100 μL of the bacterial suspension of groups (1)-(8) was spread on the agar culture plate and incubated at 37 ℃ for 24 h to observe the number of colonies.

The biofilms formed after different treatments were immersed in 2.5 % glutaraldehyde. After 12 h, they were gradually dehydrated with ethanol for 5 min each with increasing ethanol concentrations (10 %, 30 %, 50 %, 70 %, 70 %, 30 %, 50 %, 70 % and 90 %) before observation by SEM.

2.8. In vivo animal experiments

The *in vivo* animal experiments were approved by the Peking University Biomedical Ethics Committee Experimental Animal Ethics Branch (Approval number: PUIRB-LA2024192). The SD rats were purchased from Weitong Lihua Laboratory Animal Technology Co., Ltd. The weight of the 24 SD sterile mice used in the subcutaneous implantation experiments was about 50 g, and that of the 24 SD sterile rats used in the bone marrow implantation experiments was about 250 g. All the animals were kept for 7 days to acclimatize to the environment. The mice and Rats were divided into four groups randomly: (1) Puer Ti + NIR, (2) Ti@*S. mutans* + NIR, (3) 0.5 % H_2O_2 + Cu-SAE + NIR, and (4) 3 % H_2O_2 + NIR.

2.8.1. In vivo photothermal activity

The mice were anesthetized with isoflurane. Their backs were shaved, and then a 6–8 mm incision was made in the dorsal skin of the mice using a sterile scalpel. Pure titanium treated with a scavenging solution containing 0.5 % H_2O_2 and 250 μg/mL Cu-SAE were implanted into the wounds of the different groups of mice, respectively, and all of the above implants were exposed to NIR light (0.5 W·cm^{-2}, 808 nm) for 5 min.

2.8.2. In vivo biocompatibility and anti-infective properties

The mice were anesthetized with isoflurane. Their backs were shaved, and then a 6–8 mm incision was made in the dorsal skin of the

mice using a sterile scalpel. Pure titanium sheets, titanium infected by *S. mutans*, stained titanium treated with a scavenging solution containing 0.5 % H_2O_2 and 250 μg·mL^{-1} Cu-SAE, and stained titanium treated with 3 % H_2O_2 were implanted into the wounds of the different groups of mice, respectively, and all of the above implants were exposed to NIR light for 5 min. At 1 week after surgery, the titanium implants were diluted and spread on agar plates, and then inverted and placed in an anaerobic incubator for 1 day, after which the number of colonies generated was observed and counted to determine the early stage of infection. The antibacterial ratio was calculated by the following equation: Antibacterial ratio (%) = (C_0-C_1/C_0) × 100 %, where C_0 represents the number of colonies in Ti@S and mutans + NIR group and Nc refers to the number of colonies in the treated (0.5 % H_2O_2 + Cu-SAE + NIR and 3 % H_2O_2 + NIR) groups. At 4 weeks after surgery, blood (0.5 mL) was collected from the tail vein of the mice using a syringe and analyzed for hematology. The skin samples on the mice were dissected for histopathological hematoxylin and eosin (H&E) staining analysis. Additionally, the mice in each group were dissected, and the main organs (heart, liver, spleen, lung, and kidney) were collected for H&E staining to assess biosafety.

2.8.3. *In vivo osteogenesis*

The mice were anesthetized with isoflurane. Pure titanium rods, titanium infected by *S. mutans*, stained titanium treated with a scavenging solution containing 0.5 % H_2O_2 and 250 μg·mL^{-1} Cu-SAE, and stained titanium treated with 3 % H_2O_2 were implanted into femurs of the different groups of mice, respectively, and exposed to NIR for 5 min. At 1 week after surgery, the titanium implants were diluted and spread on agar plates and then inverted and placed in an anaerobic incubator for 1 day to verify the biofilm removal ability. In addition, samples were taken from the implant sites of the mice and analyzed by H&E staining. At 8 weeks post-operation, CBCT analysis was performed at the implant site of the mouse femur, and values such as bone trabeculae were quantified to assess the osteogenic capacity of the materials.

2.9. *Statistical analysis*

One-way analysis was performed using GraphPad Prism 5 statistical software packages to analyze statistically the significant differences (p) between the various groups ($p < 0.05$ represented as "*", $p < 0.01$ as "**", $p < 0.001$ as "***", and $p < 0.0001$ as "****").

3. Results and discussion

3.1. *Preparation and characterization of metal-containing single-atom nanozymes*

ZIF-8 crystals were prepared using the solvothermal method (Fig. S1) and then pyrolyzed and acid-washed at 900 °C to obtain NPC-900. The M-SAE samples were prepared using the adsorption–pyrolysis–etching method to introduce Group IB metal elements (Cu, Ag, and Au) into NPC-900 as catalytically active sites (Fig. 1**a**). As observed in TEM images, Cu-SAE, Ag-SAE, and Au-SAE all had a regular polyhedral shape, and no obvious clusters or particles were present on them (Fig. 1**b**). The atoms of each metal element were uniformly distributed throughout their respective M-SAEs. To analyze more accurately whether the metal dopants on the surface of each group of M-SAEs existed in the form of monatomic atoms, the samples were characterized using high-angle annular dark-field scanning transmission electron microscopy (AC-HAADF-STEM). In the microscopy images in Fig. 1**b**, the bright dots marked by red circles correspond to metal atoms with atomic numbers larger than those of the backing carbon atoms. The results indicated that the respective metals (Cu, Ag, and Au) in each group of M-SAEs were indeed incorporated into the C–N carriers in the form of monatomic atoms. The XRD spectral pattern of NPC-900 showing the graphitic carbon (002) and (101) crystal planes (Fig. 1**c**) suggested that ZIF-8 was completely carbonized at 900 °C [43]. The XRD spectrum of each of the three M-SAEs was consistent with that of NPC-900, with only the characteristic peaks of graphitic carbon being detected and those of the metal or metal oxide (M-oxide) not detected (Fig. 1**c**).

According to the ICP-OES results, the Cu, Ag, and Au concentrations in Cu-SAE, Ag-SAE, and Au-SAE were 56.04, 50.97, and 51.16 mg·L^{-1}, respectively, which were all within the 50–60 mg·L^{-1} range, indicating that the metal mass ratios of the three M-SAE groups were of the same order of magnitude. The number of defects and degrees of graphitization of NPC-900 and the M-SAEs were analyzed using Raman scattering spectroscopy (Fig. 1**d**). The D band represents the degree of defects, whereas the G band indicates the degree of graphitization. Generally, a larger I_D/I_G value indicates a higher degree of defects in the material [44,45]. Similar to NPC-900, each M-SAE group showed the D band at 1300 cm^{-1} and the G band at 1650 cm^{-1}, indicating that the nanozymes used NPC-900 as the carbon skeleton and the basic chemical bonds and defects had not changed significantly after metal doping. Moreover, the I_D/I_G ratios for NPC-900, Cu-SAE, Ag-SAE, and Au-SAE were 1.30, 1.44, 1.39, and 1.33, respectively (Table S1), further indicating that metal doping did not affect the number of defects in the materials. XPS was performed to determine the elemental compositions and chemical states of the M-SAE samples. Valence analysis was performed after fitting the metal elemental split peaks of the M-SAE samples (Fig. 1 **e–g**), with the results revealing that Cu in Cu-SAE coexisted in the monovalent (962.9, 942.1 eV) and divalent forms (954.7, 934.5 eV), Ag in Ag-SAE existed in the monovalent configuration only (373.8, 367.9 eV), and Au in Au-SAE coexisted in the zero (88.84 eV) and trivalent forms (91.87 eV). The above results demonstrate that the metal was successfully doped into the material matrix, while maintaining the structural integrity of the samples.

The coordination of metal atoms in different samples determines the physicochemical properties of the materials and is analyzed using X-ray absorption near-edge structure (XANES) and X-ray absorption fine structure (XAFS) spectroscopies. To analyze the metal coordination of the various M-SAEs, the coordination of the corresponding metallic elements (Cu/Ag/Au foil, M-foil) and M-oxides (CuO, Ag_2O, and Au_2O_3) were compared. The XANES spectra are shown in Fig. 2**a–c**. As seen in the zoomed-in images, the K-edge of each M-SAE lies between those of the M-oxide and M-foil, indicating that the coordination of the metal atoms had changed, resulting in a new observed coordination mode. The first derivative of the XANES spectra better characterizes the K-edge shift in M-SAE [46]. By graphing the first derivatives of each group (Fig. S2), it is observed that the edge positions of Cu-SAE, Ag-SAE, and Au-SAE are positively shifted relative to their respective metal foils, yet remain below the edge positions of the corresponding high-valent oxides. These findings are consistent with our initial linear combination fitting (LCF) and EXAFS analysis.

Extended EXAFS spectroscopy was used to determine the coordination distribution of absorbed atoms. As evident from the Fourier-transformed EXAFS spectra of the different samples (Fig. 2**d–f**), the peak positions of each M-SAE differed significantly from those of the M-foil, with only a partial overlap with those of the M-oxide. However, the peak intensities and widths changed, suggesting that the coordination numbers, bond lengths, and atomic vibration modes of the metal atoms in the M-SAEs had changed, which was consistent with the XANES results. The fitted EXAFS results are presented in Table S2 and S3. Wavelet transformation was applied to confirm the coordination of atoms around the metal atom. Different coordinating elements exhibit distinct oscillation patterns in the k-space. The strongest oscillations in the k-space occur at lower wave numbers for light elements, whereas they occur at higher wave numbers for heavy elements [47,48]. Further analysis of the coordination environment around metal atoms was conducted using wavelet transform (WT) (Fig. 2**g**). Compared with the WT patterns of corresponding M-oxides (Fig. S3), the intensity distribution of M-SAEs in the low-R, low-k region shows some similarity to oxides. However, the high-k region lacks typical M-O or M-M scattering features [49–51],

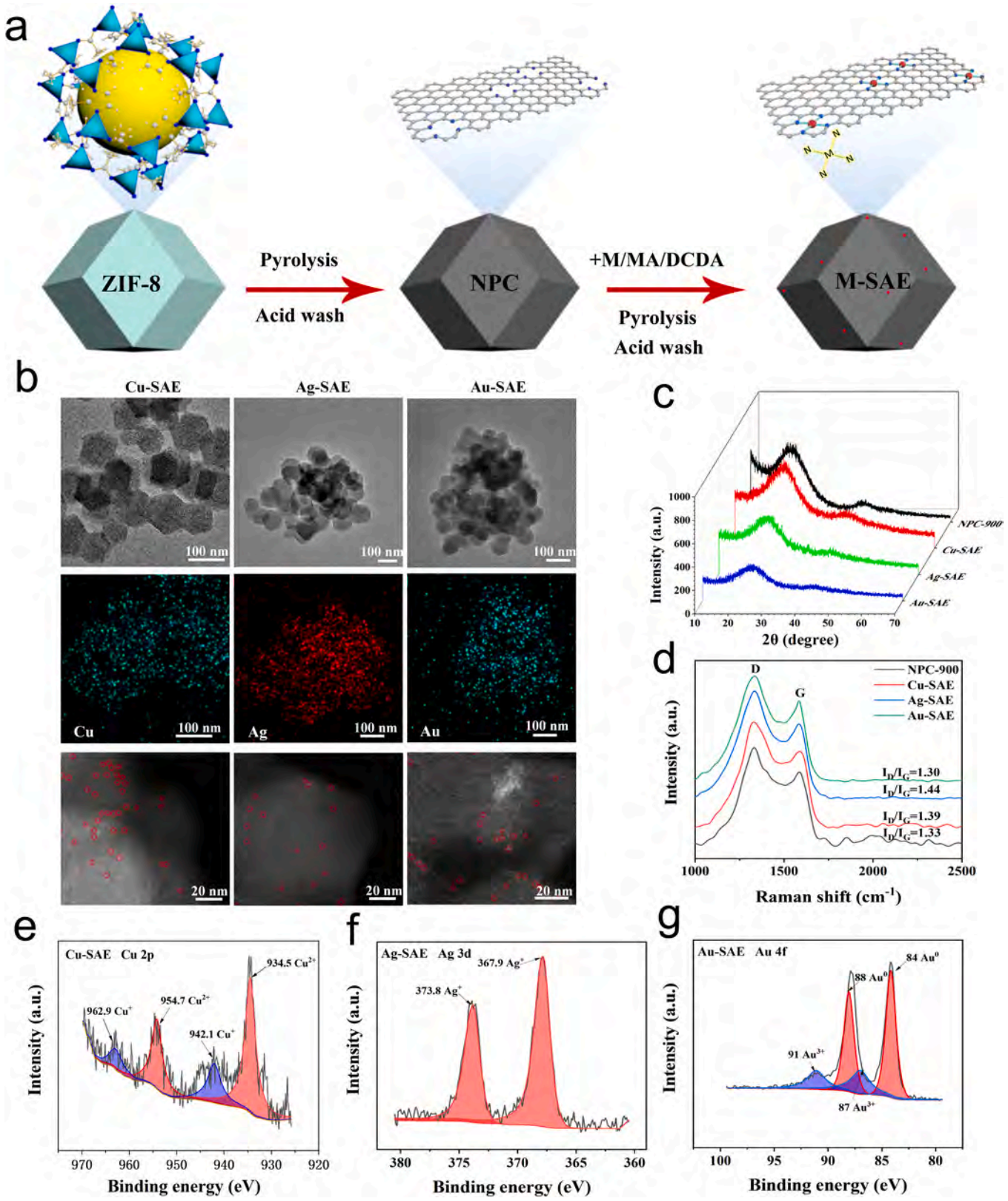

Fig. 1. Characterization of the metal-containing single-atom nanozyme (M-SAE) samples. (a) Schematic illustration of the preparation of NPC-900 and M-SAEs; (b) TEM images, corresponding elemental maps, and AC-HAADF-STEM images of Cu-SAE, Ag-SAE, and Au-SAE; (c) XRD pattern and (d) Raman scattering spectra of NPC-900 and M-SAE; (e–g) XPS high-resolution spectra of the M-SAEs: (e) Cu 2*p* of Cu-SAE, (f) Ag 3*d* of Ag-SAE, and (g) Au 4 *f* of Au-SAE.

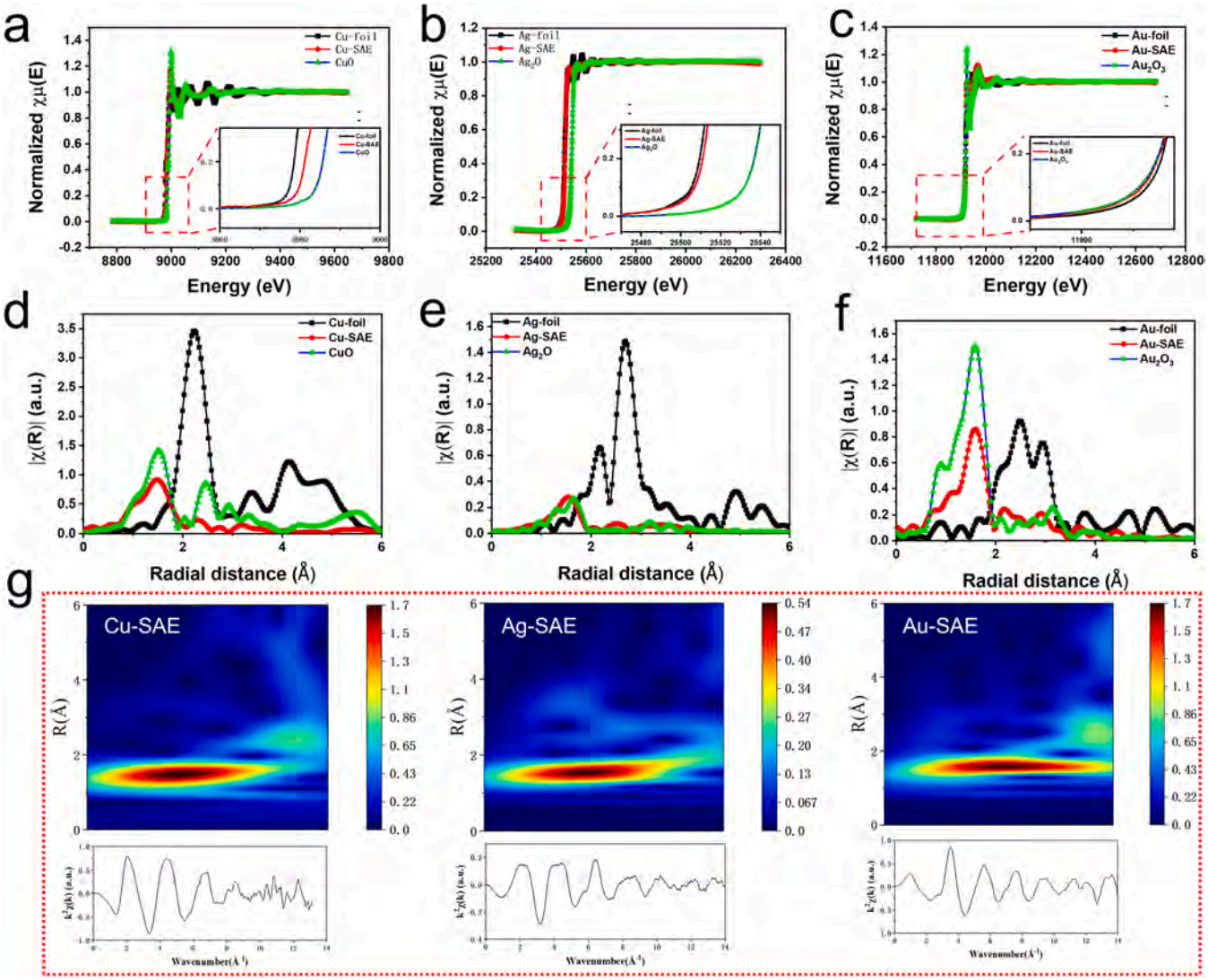

Fig. 2. XANES of (a)Cu-SAE, (b)Ag-SAE and (c)Au-SAE. Fourier-transformed EXAFS of (d)Cu-SAE, (e)Ag-SAE and (f)Au-SAE. (g) EXAFS spectra of Cu-SAE, Ag-SAE, and Au-SAE.

indicating that their local structure is not a simple replication of oxides. Specifically, the peaks of the first coordination shell appeared at (1.55 Å, 5.25 $Å^{-1}$) for Cu-SAE, at (1.55 Å, 5.75 $Å^{-1}$) for Ag-SAE, and at (1.55 Å, 7.15 $Å^{-1}$) for Au-SAE. Comparing the WT reference peaks for M-oxides and metal foils reveals that these signals primarily correspond to the contribution from N-coordination. Consequently, the following inferences could be made: N atoms are present in the first coordination shells of the M-SAE samples; the coordination forms of all M-SAEs are different from those of their corresponding metallic elements and M-oxides; and the first coordination shell consists of four N atoms in the form of M1–N4.

3.2. Photothermal conversion efficiency and enzyme-like activities of the nanozymes

SAEs have great potential for application in antimicrobial therapy and biofilm scavenging owing to their unique catalytic properties. The POD-like activities of NPC-900 and the three M-SAE constructs were evaluated using H_2O_2 as the substrate and OPDA and TMB as hydroxyl radical (•OH) indicators (Fig. 3**a**). •OH oxidizes OPDA and TMB to OPDAox and TMBox, respectively, producing absorption peaks at 452 and 652 nm in the UV spectrum. When OPDA was used as the probe, the 452 nm peak was absent in the control, weak in the NPC-900, and strong in the M-SAE samples from each group, indicating that each type of nanozyme had excellent POD activity (Fig. 3**b**). When TMB was used as the probe, the 652 nm peak was absent in the control sample and significantly stronger in each M-SAE sample than in the NPC-900 sample (Fig. 3**c**). The strength of POD activity followed the order Cu-SAE > Ag-SAE > Au-SAE > NPC-900. Enzymatic activity is usually affected by pH. The activity of most enzymes is stronger under acidic conditions and lower at other pH values because enzymes are more active under acidic conditions. The POD activity of each group of samples was evaluated at pH 3.6–7.4 (Fig. 3**d**). Compared with the control, both NPC-800 and the M-SAEs showed good POD-like activities under acidic conditions, with lower pHs resulting in higher absorbance values at 652 nm, indicating that the materials produced more ROS. The sensitivity of the samples to ambient pH varied. At pH 5.5, the activity of Cu-SAE was slightly higher than those of Ag-SAE and Au-SAE.

The large amount of •OH produced by the nanozymes can be consumed by glutathione (GSH), which is oxidized to glutathione disulfide (GSSG) in the reaction, thus reducing the damage caused by ROS to bacteria. For practicality in antibacterial scenarios, materials must have the ability to degrade GSH and prevent a large loss of ROS catalyzed by the materials in the presence of GSH. The amount of GSH consumed by each group was evaluated using the DTNB needle method. The results showed that Cu-SAE completely consumed GSH after 0.5 h,

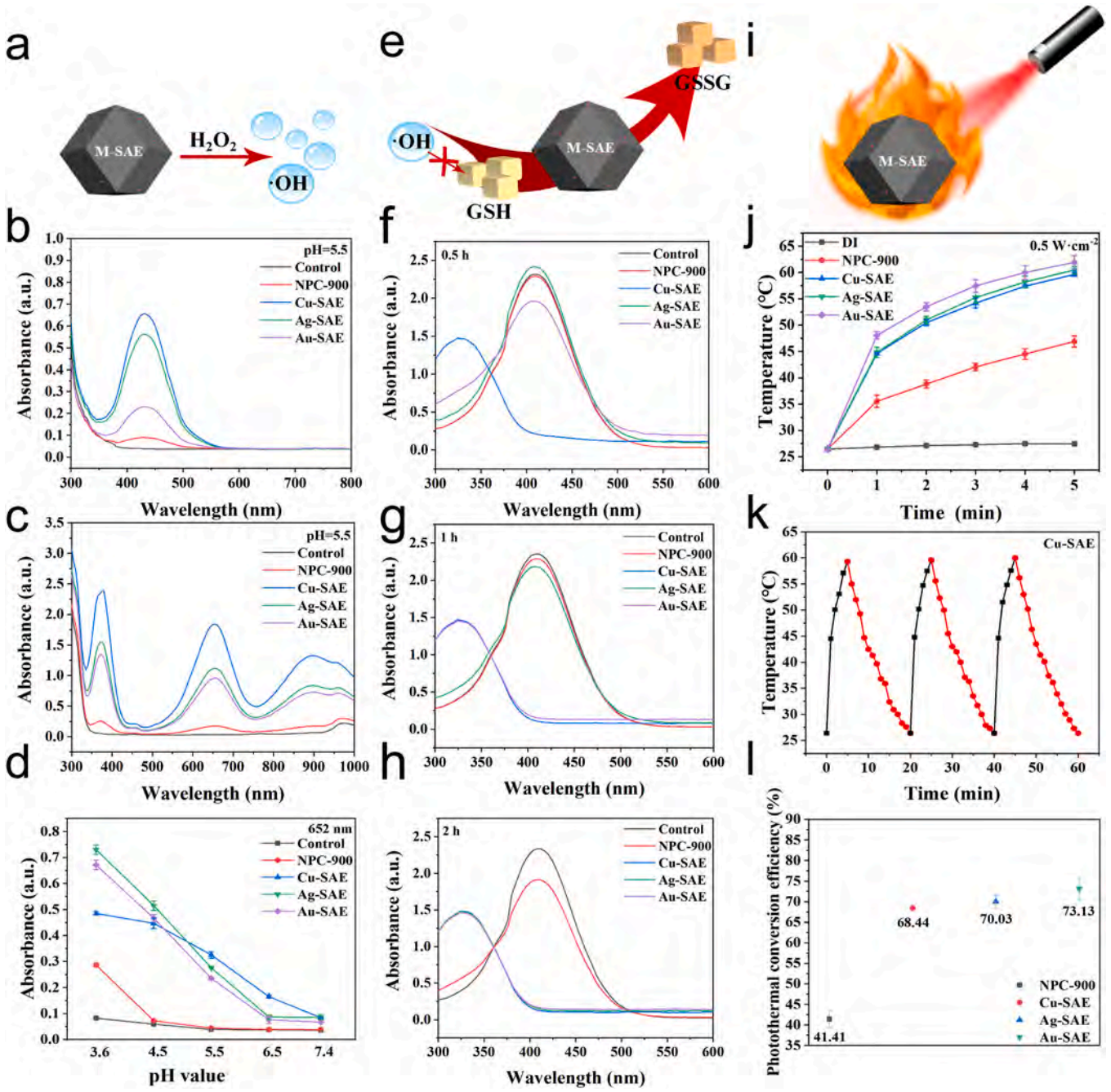

Fig. 3. Enzyme-like catalytic activities and photothermal conversion properties of NPC-900 and the various M-SAEs. Peroxidase-like activities: (a) Schematic illustration; Qualitative analysis using (b) OPDA and (c) TMB as probes; (d) Corresponding pH sensitivity. Glutathione (GSH) depletion function: (e) Schematic illustration; GSH consumption at (f) 0.5 h, (g) 1 h, and (h) 2 h using DNTB as a probe. Photothermal properties: (i) Schematic illustration; (j) Temperature-increasing curves upon 808 nm near-infrared light irradiation (0.5 W·cm^{-2}, 5 min); (k) Photothermal stability of Cu-SAE; (l) Photothermal conversion efficiency of the samples.

when the DTNB peaks nearly disappeared (Fig. 3**f**). Au-SAE showed a similar effect after 1 h (Fig. 3**g**), whereas Ag-SAE and NPC-900 exhibited lower DTNB peaks after 2 h (Fig. 3**h**), suggesting that they also possessed some GSH-consuming ability. The GSH-degrading ability of each group followed the order Cu-SAE > Au-SAE > Ag-SAE > NPC-900. In summary, the M-SAE samples, especially Cu-SAE, exhibited highly efficient GSH-consuming performance.

Good NIR light absorption is a basic requirement for photothermal reagents (Fig. 3**i**). Upon irradiation with 808 nm NIR light at a power of 0.5 W·cm^{-2}, the NPC-900 dispersion warmed to 45 ℃ in 5 min, whereas the M-SAE samples heated up to approximately 60 ℃ under the same conditions, showing a 1.5-fold higher heating rate than that of NPC-900 (Fig. 3**j**). This phenomenon occurs because the increase in metal impurity energy levels on the surface of the M-SAE samples enhances dielectric absorption and induces plasma resonance on the metal surface, resulting in stronger light absorption at 808 nm [52]. After three laser on/off cycles, the temperature increase and maximum temperature of Cu-SAE did not change significantly (Fig. 3**k**), indicating its excellent photothermal stability. The photothermal conversion efficiencies of Cu-SAE, Ag-SAE, and Au-SAE were 68.44 %, 70.03 %, and 73.13 %, respectively, which were significantly higher than that of NPC-900 (41.41 %) (Fig. 3**l**).

3.3. Catalytic mechanism of the nanozymes

To evaluate the POD activities of NPC-900 and each M-SAE construct as well as their rates of H_2O_2 adsorption/desorption, kinetic analysis was performed and the V vs. [s] and 1/V vs. 1/[s] curves were obtained with H_2O_2 as the substrate at gradient concentrations of 0–1 mM. The POD activities of the samples followed the order Cu-SAE > Ag-SAE > Au-SAE > NPC-900 (Fig. 4**a)**, which is in agreement with the results using TMB and OPDA as indicator probes. To more intuitively show the enzymatic activity of SAE, the fitted data were processed to obtain the specific activities (SA) of three SAEs (Table S4). Cu-SAE exhibits the highest SA value, while its larger Km value results in the lowest kcat/Km ratio. Conversely, Au-SAE and Ag-SAE display lower SA values, but their smaller Km values lead to higher catalytic efficiency (kcat/Km). This discrepancy indicates a trade-off between active site density and substrate affinity, consistent with the electronic structures and DFT analysis.

The 1/V vs. 1/[s] graphs (Fig. 4**b–e)** showed that the V_{max}/K_m values of the four sample groups followed the order Cu-SAE > Ag-SAE > Au-SAE > NPC-900, indicating that the H_2O_2 adsorption/desorption efficiencies of the materials are a key factor affecting their POD-like activities.

The specific surface area, pore volume, and pore size of NPC-900 and each M-SAE construct were characterized using N_2 adsorption/desorption experiments at 77 K. As shown in Table 1, the BET surface areas of NPC-900, Cu-SAE, Ag-SAE, and Au-SAE were 811.47, 568.79, 663.10, and 726.19 $m^2 \cdot g^{-1}$, respectively. The cumulative pore volumes calculated with the Barrett–Joyner–Halenda method were 0.77, 0.73, 0.48, and 0.65 $cm^3 \cdot g^{-1}$ for NPC-900, Cu-SAE, Ag-SAE, and Au-SAE, respectively, and the average pore diameters were 27.72, 23.84, 18.61, and 19.89 nm, respectively. The specific surface area, pore volume, and pore diameter of each M-SAE construct were lower than those of NPC-900

Table 1
Specific surface areas, pore volumes, and pore sizes of NPC-900 and the various M-SAEs based on BET values.

Samples	Specific surface area ($m^2 \cdot g^{-1}$)	BJH ($cm^3 \cdot g^{-1}$)	Average pore diameter (nm)
NPC−900	811.4681	0.771971	27.7232
Cu-SAE	568.7911	0.733572	23.8365
Ag-SAE	663.0965	0.475511	18.6128
Au-SAE	726.1912	0.652589	19.8865

BHJ: Barrett–Joyner–Halenda method; BET: Brunauer–Emmett–Teller

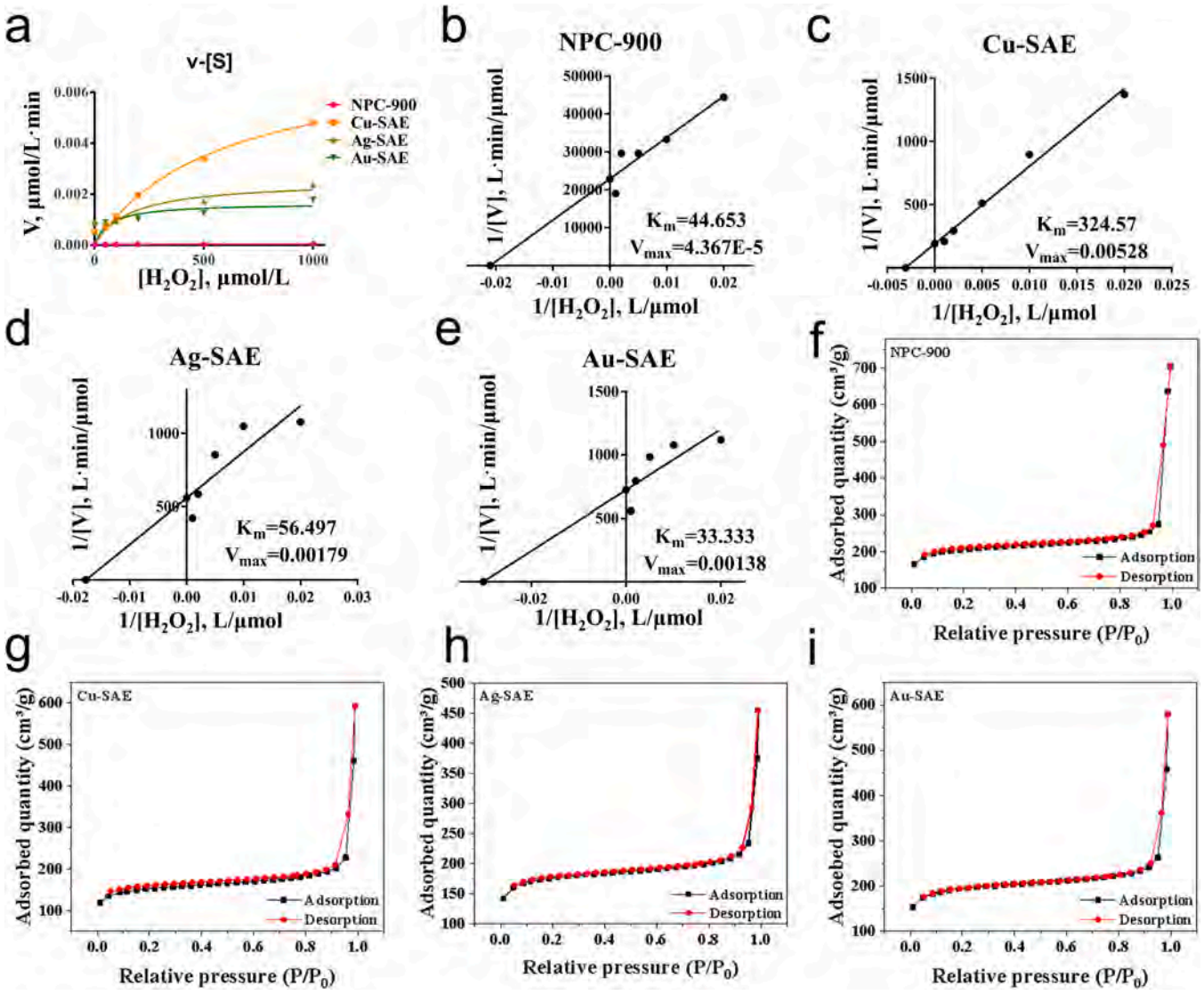

Fig. 4. (a) V vs. [s] graphs for NPC-900 and the various M-SAEs; 1/V vs. 1/[s] graphs for (b) NPC-900, (c) Cu-SAE, (d) Ag-SAE, and (e) Au-SAE (e); N_2 absorption and desorption curves for (f) NPC-900, (g) Cu-SAE, (h) Ag-SAE, and (i) Au-SAE.

because the metal dopants blocked some of the pores. NPC-900 and all the M-SAE samples exhibited similar adsorption/desorption characteristics (Fig. 4**f–i**), indicating that the basic structure of the materials had not changed after metal doping, heat treatment, and acid etching.

The larger specific surface area of carbon-based nanozymes provides more active sites for better catalytic activity [53]. However, the specific surface areas of the three M-SAE constructs were in the following order, Au-SAE > Ag-SAE > Cu-SAE. If only the size of the specific surface area is considered a factor in the POD-like activity of the M-SAE materials, the order of their catalytic activities should also be Au-SAE > Ag-SAE > Cu-SAE, which is contrary to the experimental results. Therefore, the main factors causing the difference in POD activity of these M-SAEs may be related to the number of metal centers on the surface and the electronic structure of the samples. According to the IPC-OES results, the mass ratios of the metal dopants in the M-SAE constructs were of the same order of magnitude and their metal doping concentration on the surface of the nanozymes can be regarded as being the same. Hence, the difference in POD activity among the M-SAE samples stems from the fact that the metal dopants on the nanozyme surfaces are not constant and the electronic structure of the metal centers may also be a factor.

Duan et al. [23] synthesized four types of single-atom nanomaterials with active sites of M1–N4 type, in which the metal centers were Fe, Co, Ni, or Cu. The order in which the electronic orbitals of each of these metal elements were filled was as follows: Fe: 1*s*2 2*s*2 2*p*6 3*s*2 3*p*6 3*d*6 4 *s*2; Co: 1*s*2 2*s*2 2*p*6 3*s*2 3*p*6 3*d*7 4*s*2; Ni: 1*s*2 2*s*2 2*p*6 3*s*2 3*p*6 3*d*8 4*s*2; and Cu: 1*s*2 2*s*2 2*p*6 3*s*2 3*p*6 3*d*9 4*s*2 or 1*s*2 2*s*2 2*p*6 3*s*2 3*p*6 3*d*10 4*s*1. The number of electron orbitals in these metals is consistent, with the outermost 4*s* orbitals having two electrons. However, Fe, Co, Ni, and Cu all have the same number of electron orbitals. For these four metals, the number of electrons in the penultimate 3*d* orbitals increases by 1 (from 6). Their experiments and density functional theory (DFT) simulations showed that a lower number of electrons in the *d*-band of the metal atoms correlated with a higher energy level at the center of the *d*-band and a higher capacity of the materials to adsorb H_2O_2.

Cu, Ag, and Au belong to the Group IB metals and have the following order of electron orbitals: Cu: 1*s*2 2*s*2 2*p*6 3*s*2 3*p*6 3*d*10 4*s*1; Ag: 1*s*2 2*s*2 2*p*6 3*s*2 3*p*6 3*d*10 4*s*1 4*d*10 5*s*1; and Au: 1*s*2 2*s*2 2*p*6 3*s*2 3*p*6 3*d*10 4*s*1 4*d*10 5*s*1 4*d*10 5*s*1 5*d*10 6*s*1. Although they have the same number of outermost electrons, the number of electron layers in Cu, Ag, and Au increases by one full *d*-band orbital layer in that order. Therefore, fewer

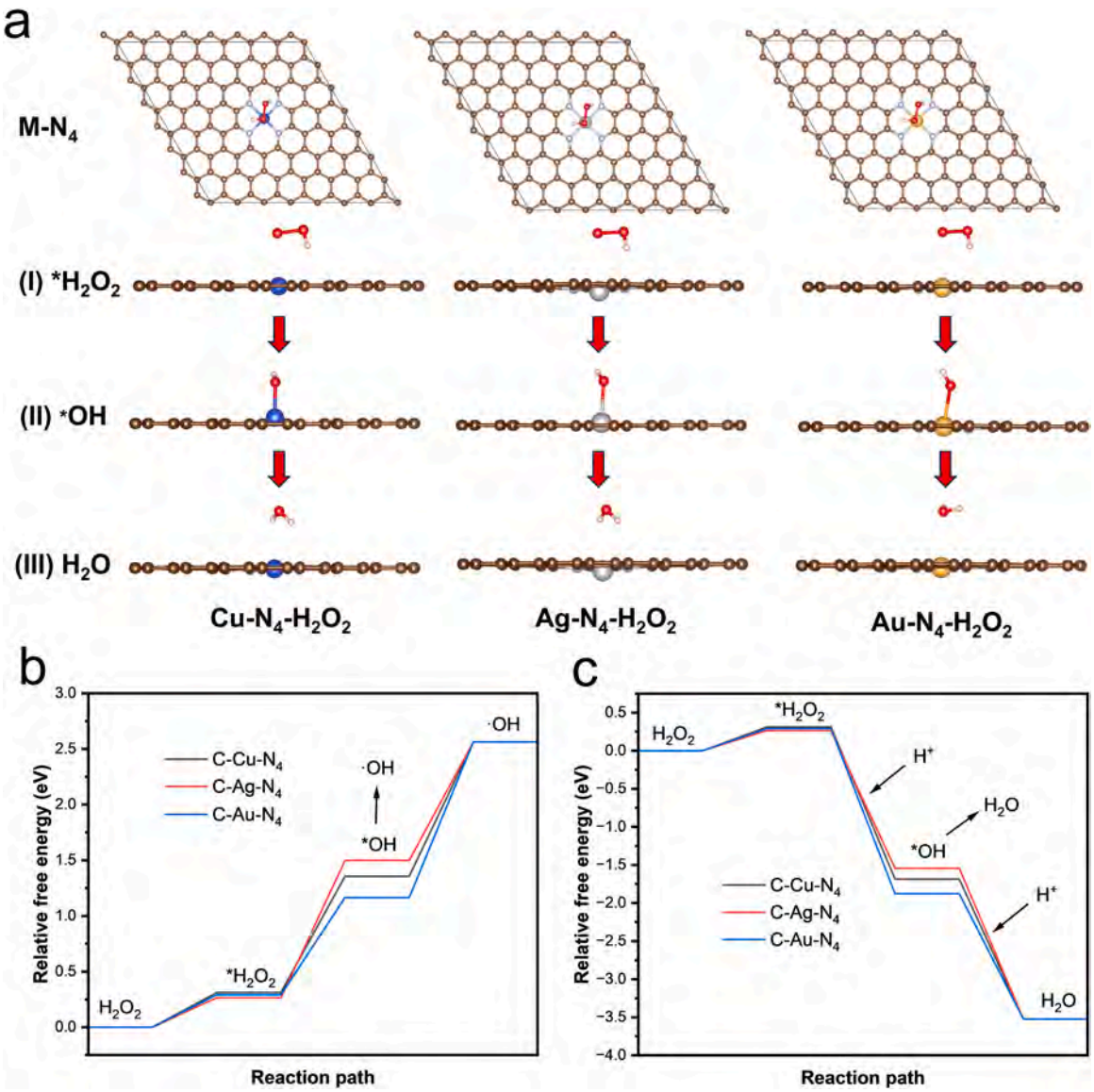

Fig. 5. (a) Density functional theory models of M1–N4 structures adsorbing and catalyzing H_2O_2; (b) Intermediate products and free energy changes of the H_2O_2 catalysis processes of different metal monoatomic enzymes at pH > 4.5; (c) Intermediate products and free energy changes of the H_2O_2 catalysis processes of different metal monoatomic enzymes at pH < 4.5.

full *d*-band orbitals correlates with a stronger coupling strength and higher energy level at the *d*-band centers, leading to a stronger capacity of the material to adsorb H_2O_2 and enhanced POD activity.

The coordination configurations of Cu, Ag, and Au as M–N₄ (M = Cu, Ag, or Au) were unambiguously confirmed using synchrotron radiation and wavelet transform analyses. To probe the catalase-like activity mechanism of these $M–N_4$ structures, DFT calculations were performed. Three periodic structural models (Cu-N_4, Ag-N_4, and Au-N_4) were constructed to simulate the catalytic H_2O_2 decomposition processes (denoted as Cu-N_4-H_2O_2, Ag-N_4-H_2O_2, and Au-N_4-H_2O_2) (Fig. 5**a**). The

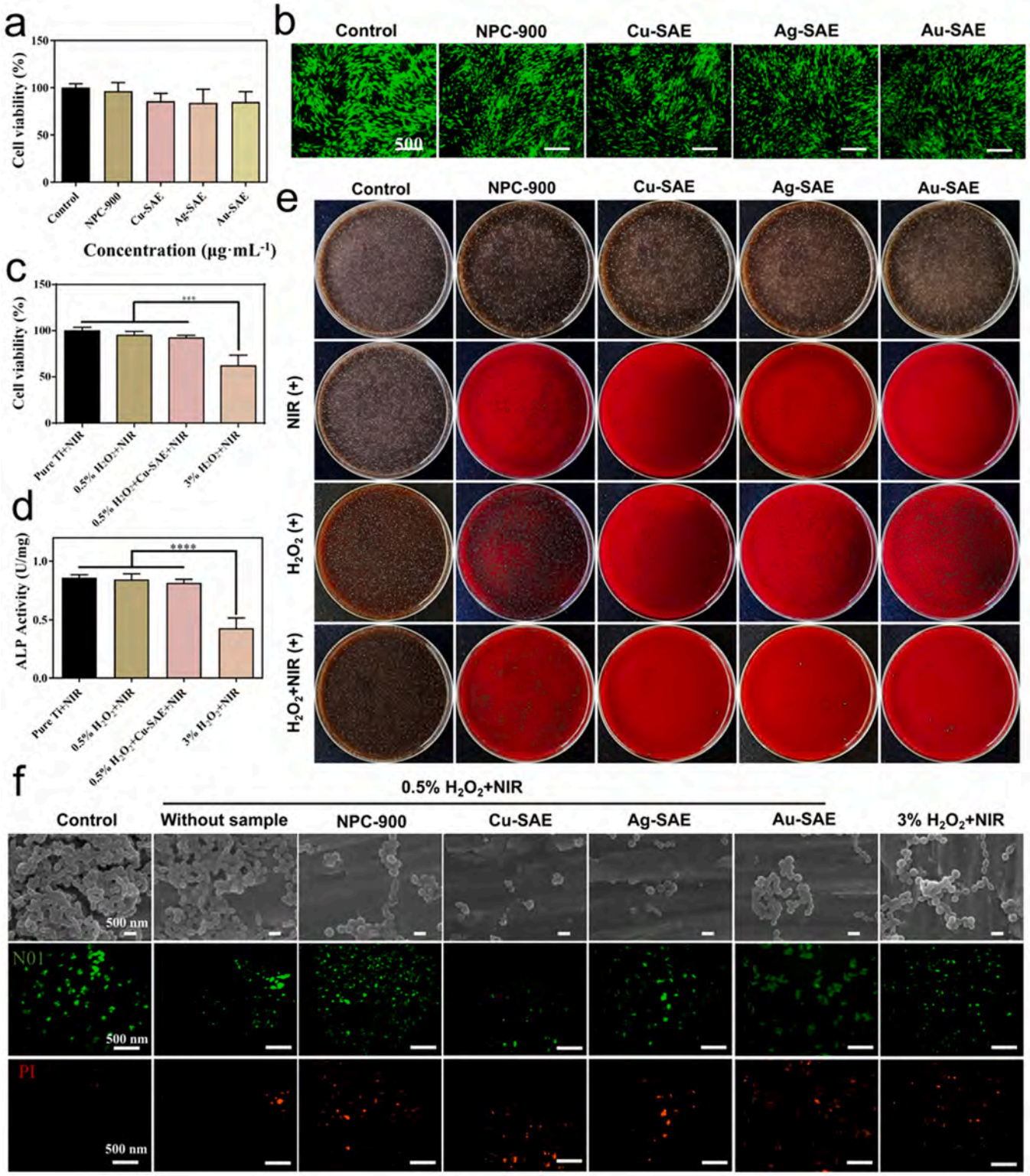

Fig. 6. (a, b) Cell viability and live/dead cell staining of hBMSCs treated with 250 μg·mL^{-1} NPC-900 or the various M-SAE constructs; (c) Viability of hBMSCs on Ti discs treated with the indicated test samples; (d) Quantitative analysis of the ALP activities of hBMSCs on Ti discs treated with the indicated test samples to determine their effects on osteogenic differentiation; (e) Images of *Streptococcus mutans* colonies after 15 min co-incubation with NPC-900 and various M-SAEs under different conditions; (f) SEM and live/dead cell staining images of *S. mutans* biofilms after treatment with NPC-900 and various M-SAEs under different conditions.

free energy profiles of the intermediate states during H_2O_2 decomposition by nanozymes are shown in Fig. 5**b**. The reaction proceeds *via* three steps: (I) H_2O_2 adsorption onto the M–N_4 active sites to form adsorbed H_2O_2 (*H_2O_2) with energy barriers of 0.312 eV (Cu-N_4), 0.261 eV (Ag-N_4), and 0.291 eV (Au-N_4); (II) dissociation of *H_2O_2 into adsorbed hydroxyl radicals (*OH), followed by their desorption; and (III) a Fenton-like reaction, where *OH radicals generate free hydroxyl radicals (•OH), the primary oxidative species, while excess *OH reacts with H^+ to form H_2O.

The primary energy barriers are in the *H_2O_2 → •OH conversion (Steps II and III), with the free energy of the final product reaching 2.562 eV. The free energy values of the *OH intermediates were 1.356 eV (Cu-N_4), 1.498 eV (Ag-N_4), and 1.165 eV (Au-N_4). The rate-determining steps and corresponding energy barriers were identified as the cleavage of the second •OH radical for Cu-N_4 (1.207 eV), that of the first •OH radical for Ag-N_4 (1.234 eV), and that of the second •OH radical for Au-N_4 (1.398 eV), leading to the catalytic efficiency order Cu-N_4 > Ag-N_4 > Au-N_4.

Under acidic conditions (increasing H^+ concentration), most *OH radicals reacted with H^+ to form H_2O before converting to •OH, thus shifting the rate-limiting step to H_2O_2 adsorption (Step I) with energy barriers of 0.312 eV (Cu-N_4), 0.264 eV (Ag-N_4), and 0.291 eV (Au-N_4). Consequently, the catalytic performance at low pH followed the order Ag-N_4 > Au-N_4 > Cu-N_4. Additionally, density of state calculations revealed that the *d*-band center values of Cu-N_4 (–3.1647 eV), Ag-N_4 (–5.1596 eV), and Au-N_4 (–6.4692 eV) correlated with the catalytic activity trends at a neutral pH, further validating the superior performance of Cu-N_4 **(**Fig. S4**)**.

3.4. Antibacterial and bone regeneration evaluations in vitro and in vivo

Hemolysis experiments were evaluated to assess the blood compatibility of each sample. The results **(**Fig. S5**)** showed that there was no significant difference in hemolysis rates between Cu-SAE, Ag-SAE and Au-SAE, which were all in a safety range (below 5 %). Then, hBMSCs were co-cultured with 250 μg·mL^{-1} of the respective test samples to further evaluate their biocompatibility. As shown in Fig. 6**a**, the viability of the cells in the presence of each test sample was more than 80 %, which was not significantly different from that of the control. Live/dead cell staining showed only green spindle-shaped live cells without red dead ones, validating the good morphology and survival status of the hBMSCs in the presence of the samples **(**Fig. 6**b)**. In conclusion, none of the samples exhibited cytotoxicity at this concentration. Although 3 % H_2O_2 can remove oral bacterial biofilms, higher concentrations can damage Ti implants and compromise cell proliferation and osteogenic differentiation. To evaluate the effects of different H_2O_2 concentrations plus 808 nm NIR light irradiation (0.5 W·cm^{-2}, 5 min) on cell viability, hBMSCs were cultured on Ti discs treated with 3 % H_2O_2, 0.5 % H_2O_2, or 0.5 % H_2O_2 + 250 μg·mL^{-1} Cu-SAE. The 3 % H_2O_2 group showed reduced cell viability (~60 %) compared with the untreated pure Ti group ($p < 0.05$) **(**Fig. 6**c)**. By contrast, both the 0.5 % H_2O_2- and Cu-SAE-containing groups maintained cell viability percentages of more than 80 %, with no significant difference compared with the pure Ti group. These findings suggest that the 0.5 % H_2O_2 + Cu-SAE combination is an implant-friendly biofilm removal strategy that can effectively minimize Ti implant damage while preserving hBMSC proliferation. To assess the effects of the different treatments on the osteogenic differentiation of cells on Ti surfaces, the ALP activity of hBMSCs was measured using ALP and BCA assay kits. The 3 % H_2O_2 group exhibited significantly lower ALP activity than that of the pure Ti + NIR group ($p < 0.05$), indicating the inhibition of osteogenic differentiation **(**Fig. 6**d)**. By contrast, the 0.5 % H_2O_2 alone and 0.5 % H_2O_2 + 250 μg·mL^{-1} Cu-SAE groups showed no significant difference in ALP activity relative to the pure Ti + NIR control, demonstrating their negligible impact on hBMSC osteogenic differentiation.

The antimicrobial efficacies of NPC-900 and the various M-SAE constructs were evaluated using representative gram-negative strains (*E. coli*) and gram-positive strains (*S. aureus* and *S. mutans*). Although NPC-900 and each M-SAE construct showed no antibacterial activity against *S. mutans*, all test samples exhibited significant antimicrobial effects when activated by 0.5 % H_2O_2 and 808 nm NIR light irradiation **(**Fig. S6, S7, **and 6e)**. Notably, compared with NPC-900, all M-SAEs delivered superior bactericidal performance, especially Cu-SAE. The combined dual stimulation (0.5 % H_2O_2 + NIR light) further enhanced the antimicrobial efficacy of each M-SAE construct, consistent with their POD activities and photothermal properties **(**Figs. 3**a–c,** 3**i–l)**. The microbiota of the human oral cavity comprises a diverse community of bacteria and fungi, among which *S. mutans* is the primary pathogenic species. Bacteria have a strong propensity to adhere to and proliferate on Ti implants, forming biofilms and causing peri-implant tissue inflammation [6]. Therefore, an ideal dental implant should not only eliminate planktonic bacteria but also possess the ability to disrupt and remove established bacterial biofilms. The effects of the different samples combined with dual stimulation (0.5 % H_2O_2 + 808 nm NIR light irradiation) on the *S. mutans* biofilm morphology were investigated using SEM and live/dead cell staining. All the treatment groups disrupted *S. mutans* biofilms after the dual stimulation treatment **(**Fig. 6**f)**. Notably, Cu-SAE resulted in the most dispersed distribution and lowest viability of the bacteria, demonstrating superior biofilm eradication capability compared with the NPC-900 and 3 % H_2O_2 treatments. Live/dead cell staining further confirmed significantly higher bacterial death in the M-SAE groups than in the NPC-900 group, with Cu-SAE showing the most potent bactericidal effect. Taken together, the results indicate that under dual stimulation, Cu-SAE achieves optimal *S. mutans* biofilm clearance and significantly outperforms the conventional 3 % H_2O_2 treatment.

The in vivo photothermal performance of the samples as shown in Fig. S8. Compared to the pure Ti, the heating rate of the Cu-SAE-treated samples was significantly enhanced. The infection control efficacies of the variously treated Ti implants were assessed using a sterile SD rat model **(**Fig. 7**a)**. At 1 week after the surgery, bacterial colonization of the explanted Ti was quantified using the plate counting method. Both experimental groups resulted in significantly reduced bacterial colony formation compared with Ti@*S. mutans* group **(**Fig. 7**b–d)**. Notably, the Ti discs treated with 0.5 % H_2O_2 + 250 μg·mL^{-1} Cu-SAE achieved an antibacterial rate of 98.58 %, significantly outperforming the 3 % H_2O_2 group (92.40 %) and indicating that the combination of 0.5 % H_2O_2 and Cu-SAE is effective in controlling early-stage infection **(**Fig. 7**b–d)**.

To further investigate the *in vivo* inflammatory responses elicited by the different treatment strategies and their biocompatibility, tissue samples from the skin wound site and major organs (heart, liver, spleen, lung, and kidney) were harvested after 4 weeks for histological sectioning and H&E staining. The H&E-stained tissues **(**Fig. 7**e)** revealed milder inflammatory cell infiltration at the wound site in the Ti@*S. mutans* + NIR group compared with that in the pure Ti + NIR group, whereas no significant inflammation was observed in either the 0.5 % H_2O_2 + Cu-SAE + NIR or 3 % H_2O_2 + NIR groups. Furthermore, no inflammatory cell infiltration or structural abnormalities were evident in the visceral organ sections **(**Fig. S9**)**, confirming that combination treatment with Cu-SAE, 0.5 % H_2O_2, and 808 nm NIR light irradiation does not induce organ damage. In summary, under 808 nm NIR light irradiation, the solution containing both Cu-SAE and 0.5 % H_2O_2 not only exhibited superior early-stage infection control (antibacterial rate > 98 %) but also mitigated the inflammatory response without causing visceral injury, thereby highlighting the outstanding *in vivo* biocompatibility and therapeutic safety of this combination treatment.

The bacterial biofilm removal and osteogenic capabilities of the variously treated Ti implants were evaluated using a sterile SD rat model **(**Fig. 8**a)**. At 1 week after the surgery, bacterial colony growth on the Ti implants was evaluated, and tissue samples from the bone wound sites were harvested for H&E staining analysis. Under NIR light illumination,

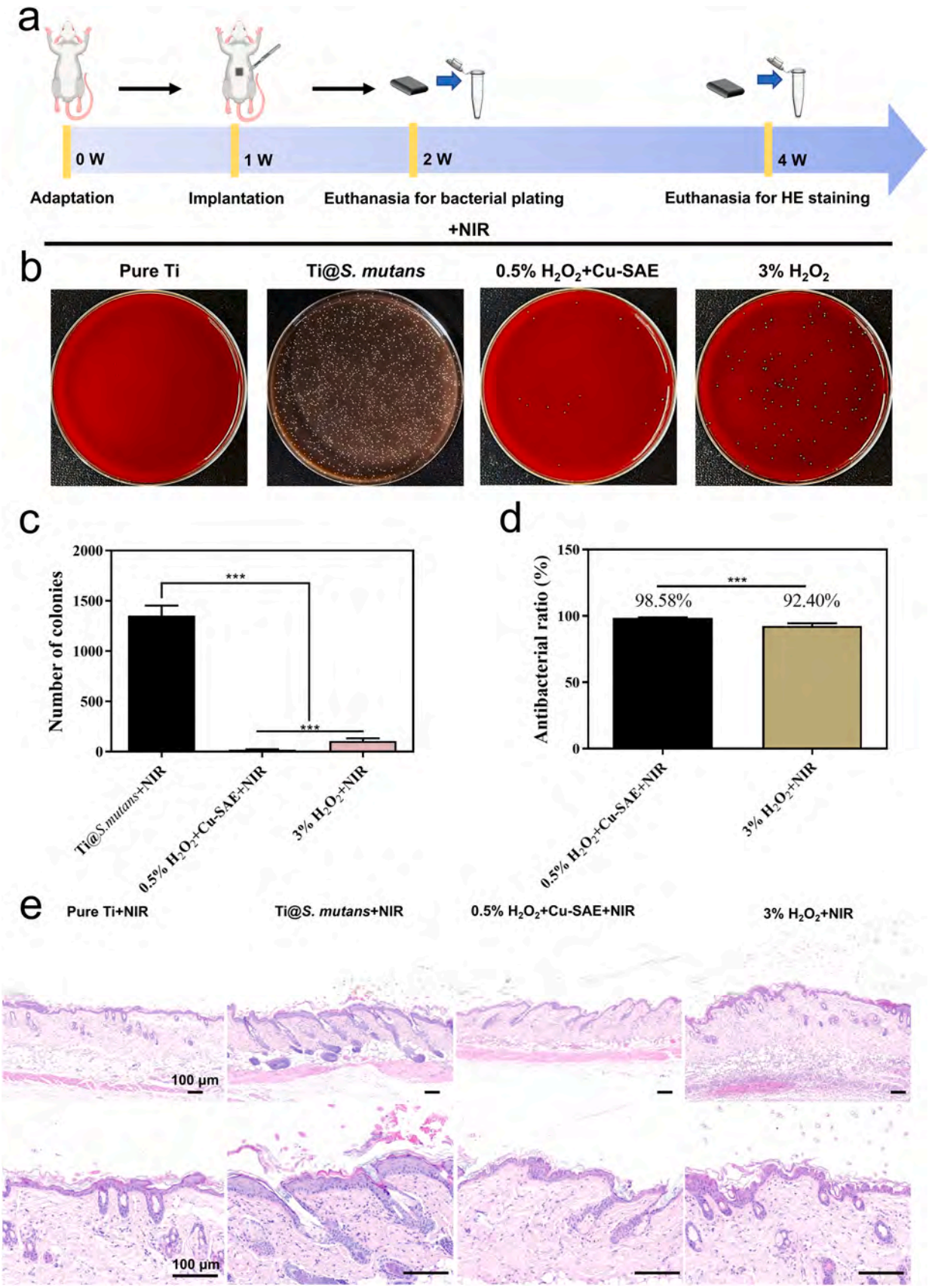

Fig. 7. (a) Schematic of the *in vivo* experiment; (b) Bacterial colonies and (c) colony counts of the various groups; (d) Antibacterial ratios of the various groups; (e) H&E-stained wounded skin of SD mice after different treatments.

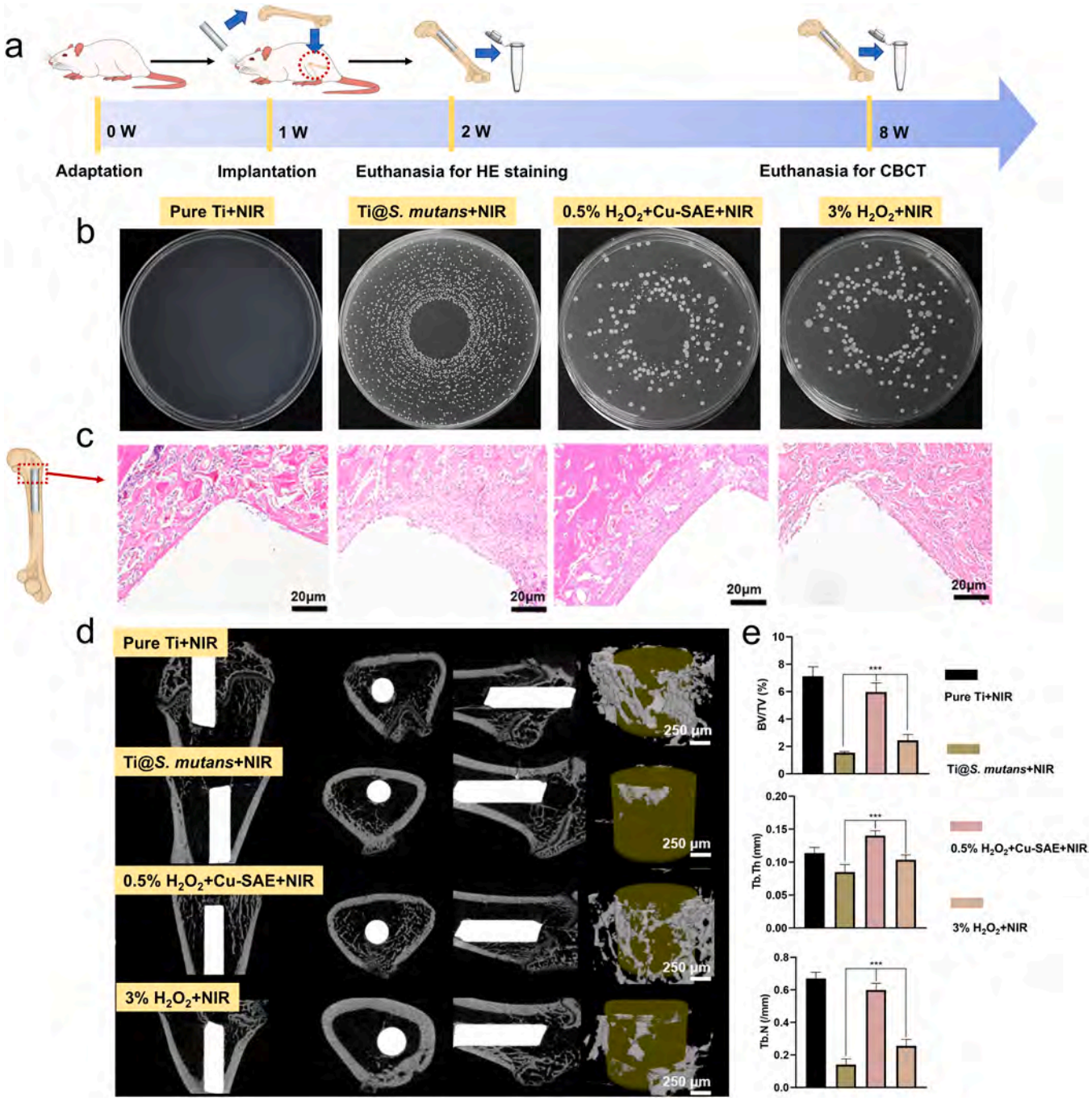

Fig. 8. **(a)** Schematic of the *in vivo* experiments; (b) Bacterial biofilm removal from different titanium rods after treating SD mice; (c) H&E staining images; (d) Micro-CT images of rat femoral defects; (e) Bone volume fraction (BV/TV), trabecular thickness (Tb.Th), and trabecular number (Tb. N) values of the various groups.

the biofilm removal efficacies of the 0.5 % H_2O_2 + Cu-SAE and 3 % H_2O_2 groups were significantly higher than that of the Ti@*S.mutans* group (Fig. 8**b**). Compared with the pure Ti group, the Ti@*S.mutans* group exhibited marked inflammatory cell infiltration, whereas such effect occurred substantially lesser in the experimental groups (Fig. 8**c**). This suggests that Cu-SAE-treated Ti implants not only possess excellent biofilm removal ability but also alleviate inflammatory responses, thereby effectively inhibiting early-stage infections. To further investigate the *in vivo* osteogenic capability of the materials, the rats were euthanized after 8 weeks for micro-CT scanning, reconstruction, and quantitative analyses. Under NIR light irradiation, the 0.5 % H_2O_2 + Cu-SAE group exhibited significantly more new bone formation than the other groups, as manifested by a larger bone volume fraction, trabecular thickness, and trabecular number (Fig. 8**d, e**). Taken together, these findings suggest that Cu-SAE not only controls infections but also has superior osteogenic capability.

4. Conclusion

ZIF-8 was used as a carbon precursor to prepare M-SAEs doped with Group IB metal elements (Cu, Ag, or Au) with an M1–N4 catalytic center structure. Experimental investigations and DFT calculations showed that Cu-SAE had superior POD-like activity, which was attributed to its smaller number of fully occupied *d*-band orbitals and the resulting higher coupling strength and energy levels of the *d*-band centers, which consequently augmented its H_2O_2 adsorption capacity. Upon dual

stimulation with low-concentration H_2O_2 and NIR light, Cu-SAE exhibited synergistic POD and photothermal capabilities as well as remarkable antibacterial efficacy against *E. coli*, *S. aureus*, and *S. mutans*. These superior properties led to the mitigation of infections on dental implants and suggest an alternative to traditional bacterial decontaminants (3 % H_2O_2). Both *in vitro* and *in vivo* experiments confirmed that the combined use of 0.5 % H_2O_2 and Cu-SAE achieves optimal antibacterial efficacy, biocompatibility, and osseointegration capability.

CRediT authorship contribution statement

Donghui Wang: Writing – review & editing, Funding acquisition, Conceptualization. **Paul K. Chu:** Writing – review & editing, Funding acquisition. **Dongdong Zhang:** Writing – original draft, Data curation, Conceptualization. **Huaiyu Wang:** Writing – review & editing, Supervision, Methodology, Funding acquisition, Conceptualization. **Lei Yan:** Conceptualization. **Ting Ma:** Writing – original draft, Data curation, Conceptualization. **Yuqing Liu:** Writing – original draft, Methodology, Investigation, Data curation, Conceptualization. **Zhaoyu Li:** Writing – review & editing. **Ye Feng:** Writing – review & editing, Data curation.

Declaration of Competing Interest

The authors declare that they have no known competing financial interests or personal relationships that could have appeared to influence the work reported in this paper.

Acknowledgments

The work was jointly supported by National Natural Science Foundation of China (52271245, 82272157, 82350710800), Natural Science Foundation of Tianjin (24JCYBJC01100), Shenzhen Science and Technology Research Funding (JCYJ20241202125205007), City University of Hong Kong Donation Research Grants (No. DON-RMG 9229021 and No. 9229021), and Guangdong - Hong Kong Technology Cooperation Funding Scheme (TCFS GHP/212/22GD and CityU 9440399).

Appendix A. Supporting information

Supplementary data associated with this article can be found in the online version at doi:10.1016/j.jallcom.2025.184299.

References

[1] W.T. Lee, J.Y. Koak, Y.J. Lim, S.K. Kim, H.B. Kwon, M.J. Kim, Stress shielding and fatigue limits of poly-ether-ether-ketone dental implants, J. Biomed. Mater. Res. B Appl. Biomater. 100 (2012) 1044–1052.
[2] G. McKenna, G. Tsakos, F. Burke, P. Brocklehurst, Managing an ageing population: challenging oral epidemiology, Prim. Dent. J. 9 (2020) 14–17.
[3] Y. Xu, Y. Li, A. Gao, P.K. Chu, H. Wang, Gasotransmitter delivery for bone diseases and regeneration, Innov. Life 1 (2023) 100015.
[4] S.E.A. Camargo, T. Roy, X. Xia, C. Fares, S.M. Hsu, F. Ren, A.E. Clark, D. Neal, J. F. Esquivel-Upshaw, Novel coatings to minimize corrosion of titanium in oral biofilm, Mater. (Basel) 14 (2021).
[5] L. Chen, Z. Tong, H. Luo, Y. Qu, X. Gu, M. Si, Titanium particles in peri-implantitis: distribution, pathogenesis and prospects, Int. J. Oral. Sci. 15 (2023) 49.
[6] A. Roccuzzo, J.C. Imber, G.E. Salvi, M. Roccuzzo, Peri-implantitis as the consequence of errors in implant therapy, Periodontology 2000 92 (2023) 350–361.
[7] F.L. Zhao, A. Gao, Q. Liao, Y.Y. Li, I. Ullah, Y. Zhao, X.X. Ren, L.P. Tong, X. Li, Y. D. Zheng, P.K. Chu, H.Y. Wang, Balancing the Anti-Bacterial and Pro-Osteogenic properties of Ti-Based implants by partial conversion of ZnO nanorods into hybrid zinc phosphate nanostructures, Adv. Funct. Mater. 34 (2024).
[8] Y. Wu, H. Wang, P.K. Chu, Enhancing macrophages to combat intracellular bacteria, Innov. Life 1 (2023) 100027.
[9] S.W. Dickey, G.Y.C. Cheung, M. Otto, Different drugs for bad bugs: antivirulence strategies in the age of antibiotic resistance, Nat. Rev. Drug Discov. 16 (2017) 457–471.
[10] Z. Du, F. Qiao, L. Tong, W. Zhang, X. Mou, X. Zhao, M.F. Maitz, H. Wang, N. Huang, Z. Yang, Mimicking mytilus edulis foot protein: a versatile strategy for robust biomedical coatings, Innovation 5 (2024) 100671.
[11] T.D. Rees, C.F. Orth, Oral ulcerations with use of hydrogen peroxide, J. Periodo 57 (1986) 689–692.
[12] K. Shetty, Hydrogen peroxide burn of the oral mucosa, Ann. Pharm. 40 (2006) 351.
[13] M.V. Marshall, L.P. Cancro, S.L. Fischman, Hydrogen peroxide: a review of its use in dentistry, J. Periodo 66 (1995) 786–796.
[14] C.B. Anfinsen, Principles that govern the folding of protein chains, Science 181 (1973) 223–230.
[15] I. Schomburg, A. Chang, S. Placzek, C. Söhngen, M. Rother, M. Lang, C. Munaretto, S. Ulas, M. Stelzer, A. Grote, M. Scheer, D. Schomburg, BRENDA in 2013: integrated reactions, kinetic data, enzyme function data, improved disease classification: new options and contents in BRENDA, Nucleic Acids Res 41 (2013) D764–D772.
[16] Z. Zeng, R. Xu, J. Guo, J. Jin, H. He, X. Luo, Accelerating functional protein discovery with GPT models: antimicrobials and enzymes, Innov. Life 3 (2025) 100133.
[17] M. Huo, L. Wang, Y. Wang, Y. Chen, J. Shi, Nanocatalytic tumor therapy by Single-Atom catalysts, ACS Nano 13 (2019) 2643–2653.
[18] X. Liu, Z. Yan, Y. Zhang, Z. Liu, Y. Sun, J. Ren, X. Qu, Two-Dimensional Metal–Organic Framework/Enzyme hybrid nanocatalyst as a benign and Self-Activated cascade reagent for in vivo wound healing, ACS Nano 13 (2019) 5222–5230.
[19] Y. Hu, H. Cheng, X. Zhao, J. Wu, F. Muhammad, S. Lin, J. He, L. Zhou, C. Zhang, Y. Deng, P. Wang, Z. Zhou, S. Nie, H. Wei, Surface-Enhanced Raman scattering active gold nanoparticles with Enzyme-Mimicking activities for measuring glucose and lactate in living tissues, ACS Nano 11 (2017) 5558–5566.
[20] H. Yu, M. Liu, X. Lu, J. Qu, G. Tao, A cooling wound dressing for accelerating healing under sunlight, Innovation 5 (2024) 100670.
[21] M. Liang, X. Yan, Nanozymes: from new concepts, mechanisms, and standards to applications, Acc. Chem. Res. 52 (2019) 2190–2200.
[22] N.A. Kotov, Chemistry. Inorganic nanoparticles as protein mimics, Science 330 (2010) 188–189.
[23] J. Duan, Y. Zhou, Y. Ren, F. Liu, P. Deng, M. Yang, H. Ge, J. Gao, J. Yang, Y. Qin, Effect of electronic structure over late Transition-Metal M1–N4 Single-Atom sites on hydroxyl Radical-Induced oxidations, ACS Catal. 13 (2023) 3308–3316.
[24] M. Tong, F. Sun, Y. Xie, Y. Wang, Y. Yang, C. Tian, L. Wang, H. Fu, Operando cooperated catalytic mechanism of atomically dispersed Cu-N(4) and Zn-N(4) for promoting oxygen reduction reaction, Angew. Chem. Int. Ed. Engl. 60 (2021) 14005–14012.
[25] Y. Wang, G. Jia, X. Cui, X. Zhao, Q. Zhang, L. Gu, L. Zheng, L.H. Li, Q. Wu, D. J. Singh, D. Matsumura, T. Tsuji, Y.-T. Cui, J. Zhao, W. Zheng, Coordination number regulation of molybdenum Single-Atom nanozyme Peroxidase-like specificity, Chem 7 (2021) 436–449.
[26] S. Ji, B. Jiang, H. Hao, Y. Chen, J. Dong, Y. Mao, Z. Zhang, R. Gao, W. Chen, R. Zhang, Q. Liang, H. Li, S. Liu, Y. Wang, Q. Zhang, L. Gu, D. Duan, M. Liang, D. Wang, X. Yan, Y. Li, Matching the kinetics of natural enzymes with a single-atom iron nanozyme, Nat. Catal. 4 (2021) 407–417.
[27] S. Sun, Y. Zhang, X. Shi, W. Sun, C. Felser, W. Li, G. Li, From charge to spin: an In-Depth exploration of electron transfer in energy electrocatalysis, Adv. Mater. 36 (2024) 2312524.
[28] S.O. Aisida, A. Batool, F.M. Khan, L. Rahman, A. Mahmood, I. Ahmad, T.-k Zhao, M. Maaza, F.I. Ezema, Calcination induced PEG-Ni-ZnO nanorod composite and its biomedical applications, Mater. Chem. Phys. 255 (2020) 123603.
[29] Y. Wang, Z. Zhang, G. Jia, L. Zheng, J. Zhao, X. Cui, Elucidating the mechanism of the structure-dependent enzymatic activity of Fe–N/C oxidase mimics, Chem. Commun. 55 (2019) 5271–5274.
[30] Y. Wang, A. Cho, G. Jia, X. Cui, J. Shin, I. Nam, K.J. Noh, B.J. Park, R. Huang, J. W. Han, Tuning local coordination environments of manganese Single-Atom nanozymes with multi-enzyme properties for selective colorimetric biosensing, Angew. Chem. Int. Ed. Engl. 62 (2023) e202300119.
[31] J. Yang, R. Zhang, H. Zhao, H. Qi, J. Li, J.F. Li, X. Zhou, A. Wang, K. Fan, X. Yan, T. Zhang, Bioinspired copper single-atom nanozyme as a superoxide dismutase-like antioxidant for sepsis treatment, Explor. (Beijing China) 2 (2022) 20210267.
[32] S. Bhattacharjee, U.V. Waghmare, S.C. Lee, An improved d-band model of the catalytic activity of magnetic transition metal surfaces, Sci. Rep. 6 (2016) 35916.
[33] R.T. Hannagan, G. Giannakakis, M. Flytzani-Stephanopoulos, E.C.H. Sykes, Single-Atom alloy catalysis, Chem. Rev. 120 (2020) 12044–12088.
[34] M.L. Ermini, V. Voliani, Antimicrobial nano-agents: the copper age, ACS nano 15 (2021) 6008–6029.
[35] L. Rizzello, P.P. Pompa, Nanosilver-based antibacterial drugs and devices: mechanisms, methodological drawbacks, and guidelines, Chem. Soc. Rev. 43 (2014) 1501–1518.
[36] X. Fan, L.H. Yahia, E. Sacher, Antimicrobial properties of the ag, cu nanoparticle system, Biology 10 (2021) 137.
[37] Q. Yang, H. Kong, L. Tang, Y. Ma, F. Liu, M. Liu, Y. Wang, P. Zhang, Y. Zheng, Au–Cu janus nanostructures as NIR-II photothermal antibacterial agents, ACS Appl. Nano Mater. 7 (2024) 20783–20792.
[38] Y. Liu, K. Ai, J. Liu, M. Deng, Y. He, L. Lu, Dopamine-melanin colloidal nanospheres: an efficient near-infrared photothermal therapeutic agent for in vivo cancer therapy, Adv. Mater. 25 (2013) 1353–1359.
[39] G. Kresse, J. Furthmüller, Efficient iterative schemes for ab initio total-energy calculations using a plane-wave basis set, Phys. Rev. B Condens Matter 54 (1996) 11169–11186.
[40] G. Kresse, D. Joubert, From ultrasoft pseudopotentials to the projector augmented-wave method, Phys. Rev. B 59 (1999) 1758–1775.
[41] J.P. Perdew, K. Burke, M. Ernzerhof, Generalized gradient approximation made simple, Phys. Rev. Lett. 77 (1996) 3865–3868.

[42] S. Grimme, J. Antony, S. Ehrlich, H. Krieg, A consistent and accurate ab initio parametrization of density functional dispersion correction (DFT-D) for the 94 elements H-Pu, J. Chem. Phys. 132 (2010) 154104.
[43] X. Wang, Q. Shi, Z. Zha, D. Zhu, L. Zheng, L. Shi, X. Wei, L. Lian, K. Wu, L. Cheng, Copper single-atom catalysts with photothermal performance and enhanced nanozyme activity for bacteria-infected wound therapy, Bioact. Mater. 6 (2021) 4389–4401.
[44] A.C. Ferrari, J. Robertson, Interpretation of Raman spectra of disordered and amorphous carbon, Phys. Rev. B 61 (2000) 14095–14107.
[45] L.G. Cançado, A. Jorio, E.H. Ferreira, F. Stavale, C.A. Achete, R.B. Capaz, M. V. Moutinho, A. Lombardo, T.S. Kulmala, A.C. Ferrari, Quantifying defects in graphene via Raman spectroscopy at different excitation energies, Nano Lett. 11 (2011) 3190–3196.
[46] W. Yin, X. Zhi, Y. Li, J. Ma, B. Johannessen, F. Xie, M. Wu, Bimetallic Alloy Air Cathode Promoting Superoxide Formation for High-Performance Na-Air Batteries, 21 (2025) 2500109.
[47] J.J. Rehr, R.C. Albers, Theoretical approaches to x-ray absorption fine structure, Rev. Mod. Phys. 72 (2000) 621–654.
[48] D.C. Koningsberger, R. Prins, X-ray absorption: principles, applications, techniques of EXAFS, SEXAFS, and XANES, X-ray absorption: principles, applications, techniques of EXAFS, SEXAFS, and XANES 1988.
[49] A. Moutsiou, A. Olivati, L.A. Cipriano, A. Sivo, S.M. Collins, Q.M. Ramasse, I. S. Kwon, G. Di Liberto, M. Kanso, R. Wojcieszak, G. Pacchioni, A. Petrozza, G. Vilé, Tracking charge dynamics in a silver Single-Atom catalyst during the Light-Driven oxidation of benzyl alcohol to benzaldehyde, ACS Catal. 15 (2025) 5601–5613.
[50] Y.-M. Wang, F.-Q. Yan, Q.-Y. Wang, C.-X. Du, L.-Y. Wang, B. Li, S. Wang, S.-Q. Zang, Single-atom tailored atomically-precise nanoclusters for enhanced electrochemical reduction of CO2-to-CO activity, Nat. Commun. 15 (2024) 1843.
[51] T. Wang, F. Zhang, C.F. Guimarães, R.L. Reis, Y. Lv, Y. Qu, D. Liu, Q. Zhou, X. Kong, J. Shi, Zn/Cu Bi-Single-Atom nanoplatform: hexagonal Anti-Tumor warrior by ROS amplification for DOX resistance reversal and, Immune Act. 34 (2024) 2410962.
[52] L. Liu, H. Zhang, S. Xing, Y. Zhang, L. Shangguan, C. Wei, F. Peng, X. Liu, Copper-Zinc bimetallic Single-Atom catalysts with localized surface plasmon Resonance-Enhanced photothermal effect and catalytic activity for melanoma treatment and Wound-Healing, Adv. Sci. (Weinh.) 10 (2023) e2207342.
[53] H. Wang, Q. Wang, Q. Wang, W. Dong, Y. Liu, Q. Hu, X. Song, S. Shuang, C. Dong, X. Gong, Metal-free nitrogen-doped carbon nanodots as an artificial nanozyme for enhanced antibacterial activity, J. Clean. Prod. 411 (2023) 137337.

Supplementary Information

Impacts of the Electronic Structures of Group IB Element-centered Single-Atom Nanozymes on their Catalytic Activities and Management of Peri-Implantitis

Yuqing Liu[a,b,1], Ting Ma[c,1] ,Ye Feng[d], Zhaoyu Li[d], Lei Yan[b], Huaiyu Wang[b,*], Dongdong Zhang[b,e*], Paul K. Chu[e], Donghui Wang[d,*]

[a] *School of Advanced Manufacturing, Fuzhou University, 1 Shuicheng Road, Jinjiang, Fujian, 362251, PR China*

[b] *Center for Human Tissues and Organs Degeneration, Shenzhen Institute of Advanced Technology, Chinese Academy of Sciences, Shenzhen 518055, China*

[c] *Department of Oral Implantology, Peking University School and Hospital of Stomatology, 22 Zhongguancun South Avenue, Haidian District, Beijing 10081, PR China*

[d] *Department of Physics, Department of Materials Science & Engineering, and Department of Biomedical Engineering, City University of Hong Kong, Tat Chee Avenue, Kowloon, Hong Kong, China*

[e] *Hebei Key Laboratory of Biomaterials and Smart Theranostics, School of Health Sciences and Biomedical Engineering, Hebei University of Technology, Tianjin 300130, China*

*** Corresponding Authors:** *donghuiwang@hebut.edu.cn (D.H. Wang); dd.zhang2@siat.ac.cn (D.D. Zhang); hy.wang1@siat.ac.cn (H.Y. Wang)*

[1] These authors contributed equally to this work

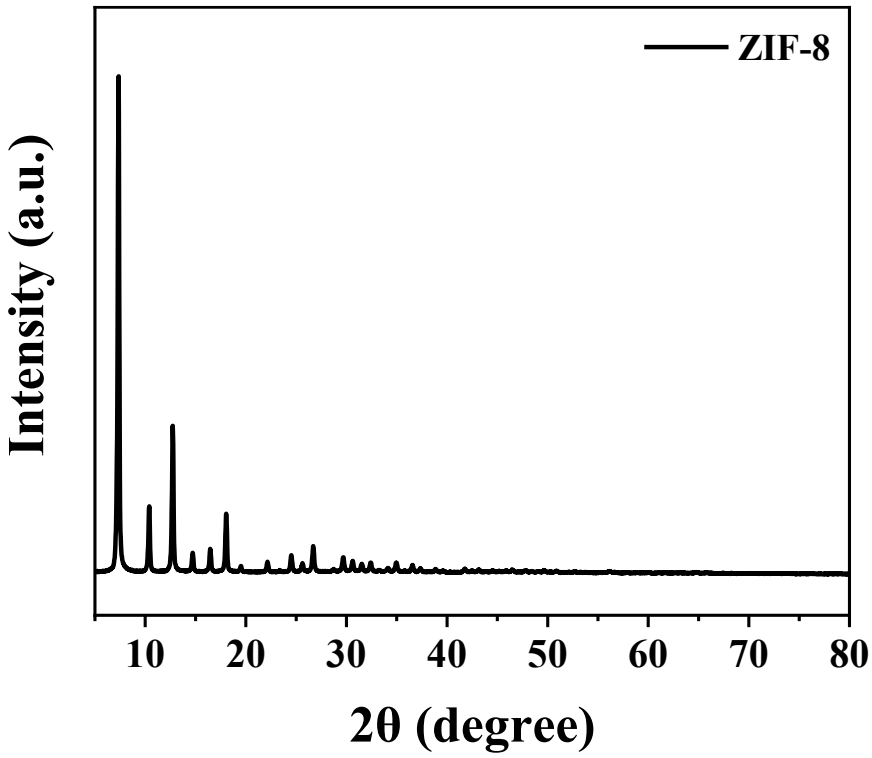

Fig. S1. XRD spectrum of ZIF-8.

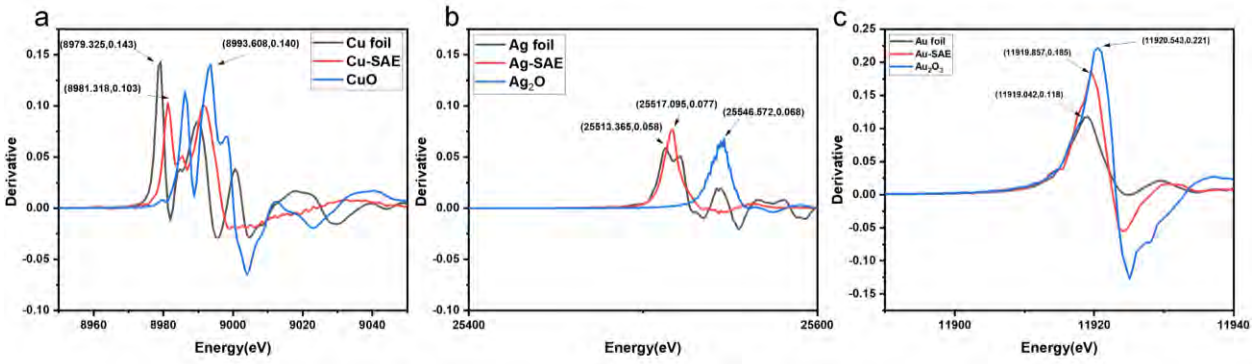

Fig. S2. First derivative of the XANES spectra for M-SAE.

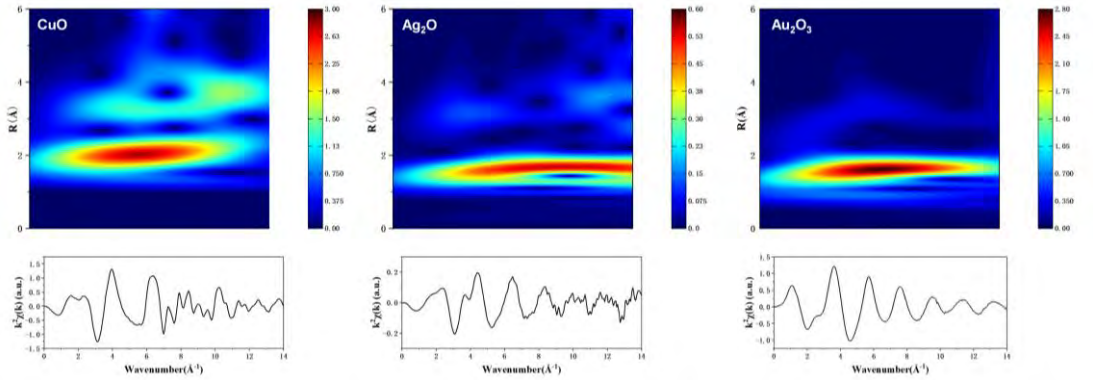

Fig. S3. Wavelet transform of the corresponding M-oxide

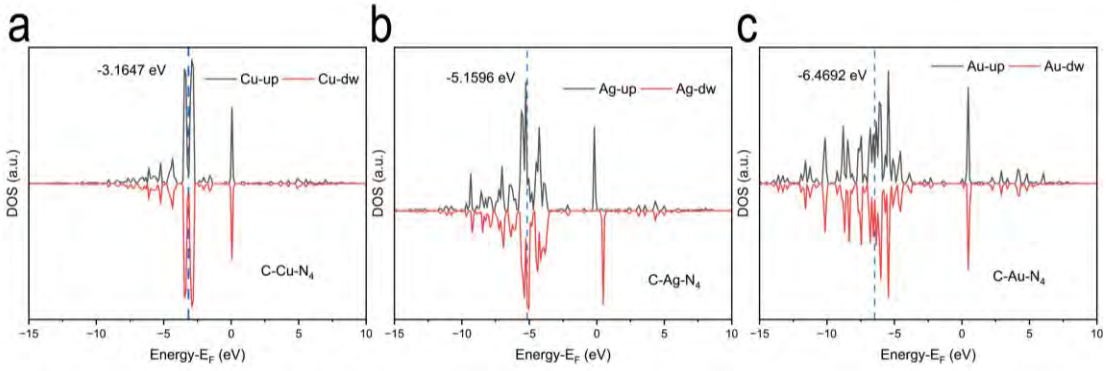

Fig. S4. Density of states (DOS) of M-N4 (M = Cu, Ag, Au) with the blue dotted line showing the D-band center of each system.

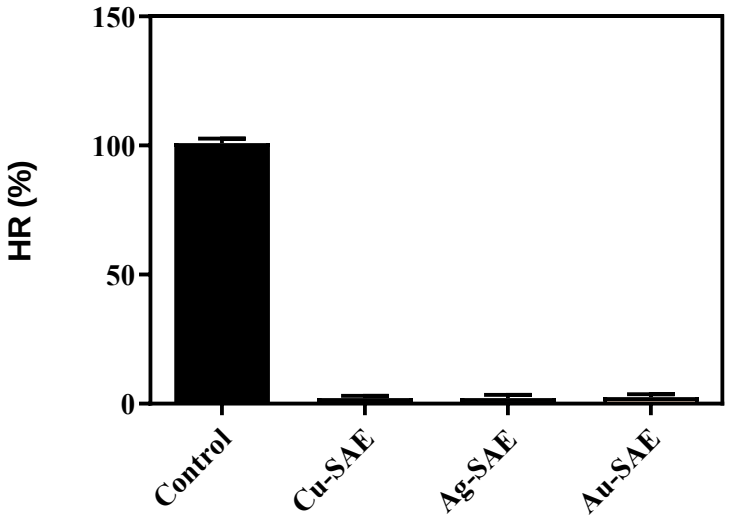

Fig. S5. Hemolysis rate of the various samples.

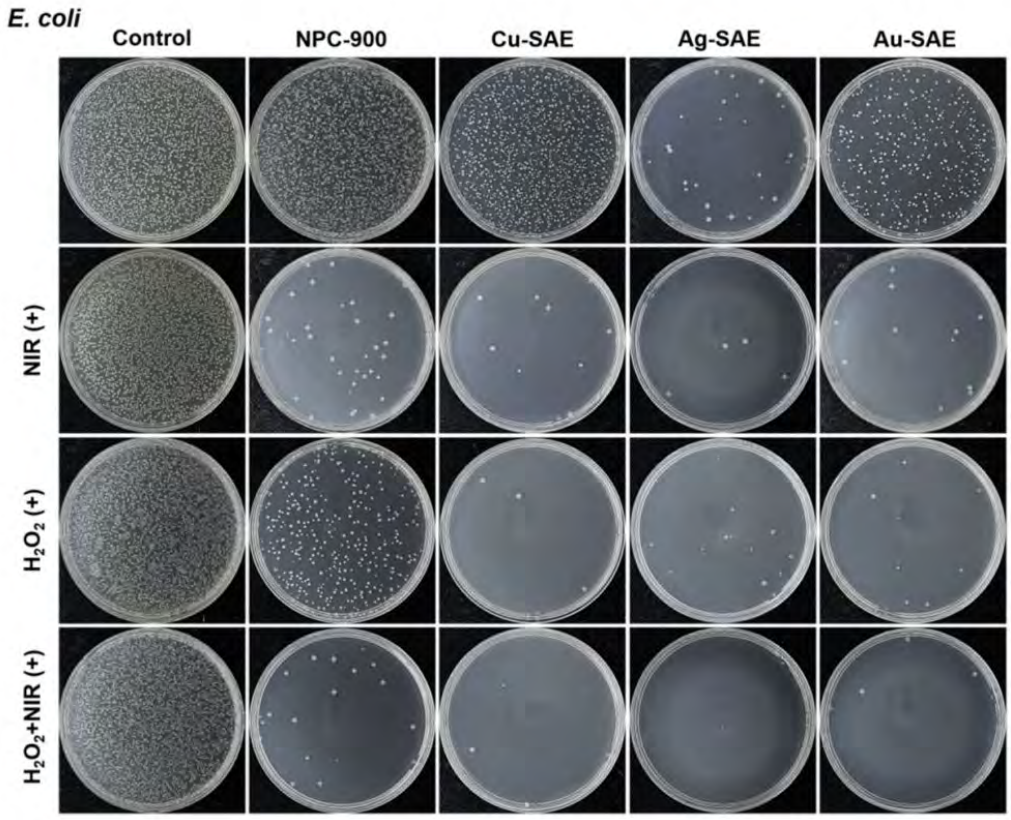

Fig. S6. Colony generation images of NPC-900 and M-SAE after co-incubation with *E. coli* for 15 minutes under different conditions.

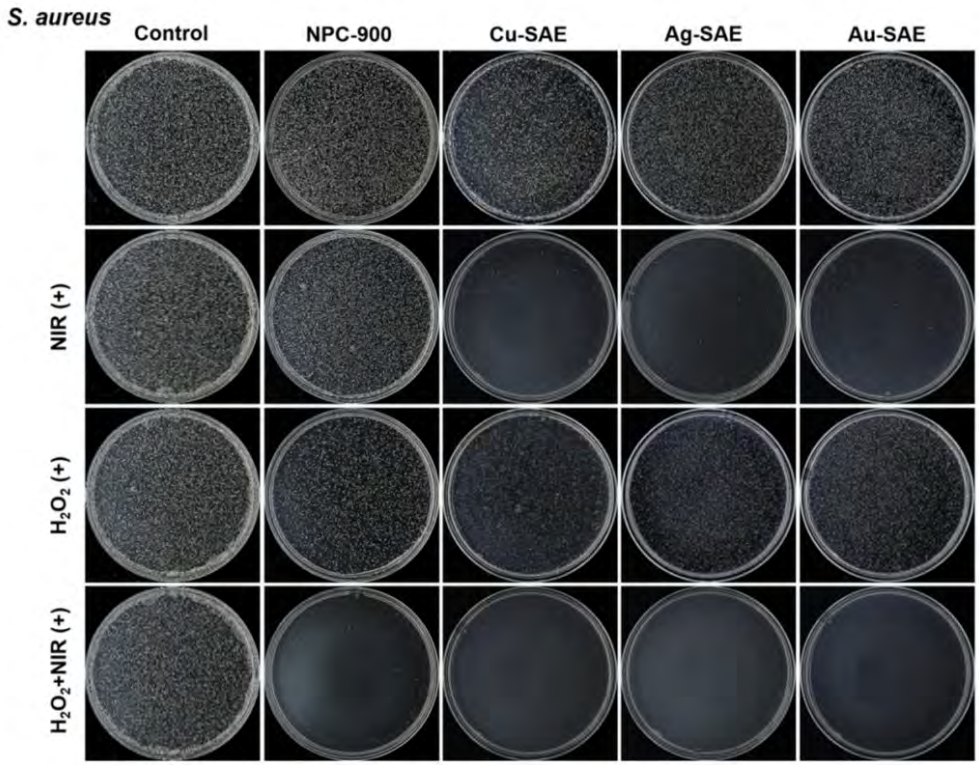

Fig. S7. Colony generation images of NPC-900 and M-SAE after co-incubation with *S. aureus* for 15 minutes under different conditions.

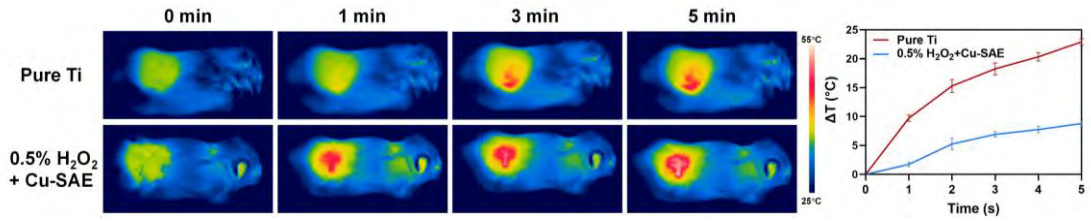

Fig. S8. The in vivo photothermal performance of the samples.

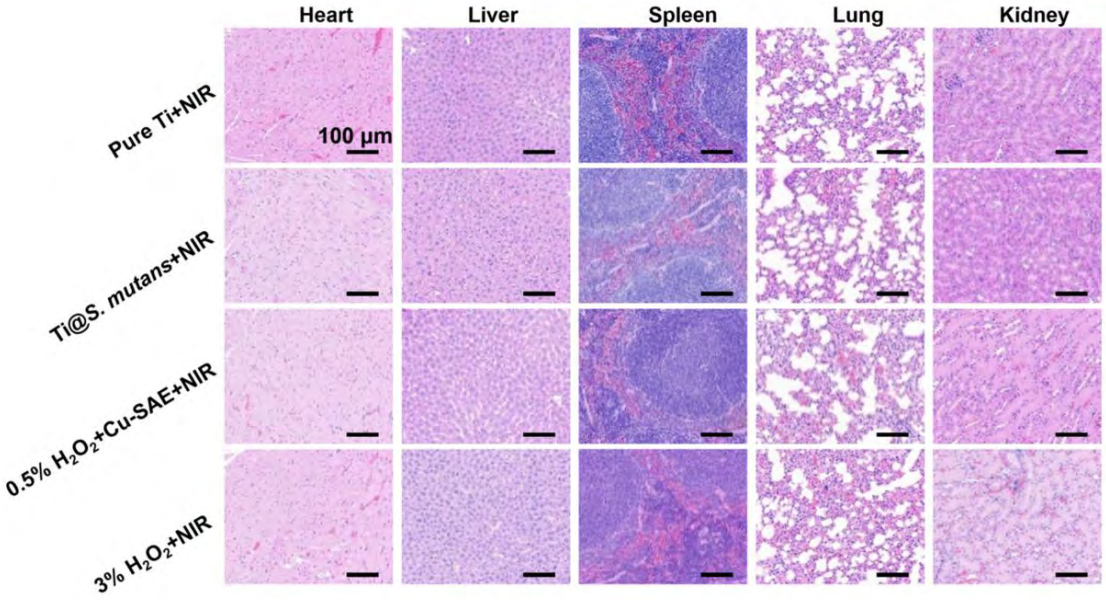

Fig. S9. H&E staining images of major organs of SD mice after different treatments.

Table S1. ID/IG ratio analysis of NPC-800 and M-SAE.

Samples	**I_D**	**I_G**	**I_D/I_G**
Au-SAE	1526.02	1173.88	1.30
Ag-SAE	1420.41	986.39	1.44
Cu-SAE	1062.35	764.29	1.39
NPC-900	796.46	598.84	1.33

Table S2. Coordination condition of M-SAE in various samples acquired from the fitting of EXAFS.

	Au-SAE	**Ag-SAE**	**Cu-SAE**
S_0^2	1.023±0.00569	0.209±0.00425	0.847±0.00743
E_0	-1.918±0.12466	8.170±0.00930	9.324±0.05205
R(M)	2.10636±0.01396797	1.97240±0.00706039	1.92965±0.02297141

N(M) = 4

Table S3. Fitting parameters and coordination path coordination path

Samples	N	Reff（Å）	R（Å）（Reff + ΔR）	ΔR（Å）	σ² （Å²))
Cu-N	4	1.982	1.93 ± 0.02	-0.052 ±0.023	0.00743±0.00345
Ag-N	4	1.9817	1.9724±0.01	-0.0093±0.0071	0.00425±0.00093
Au-N	4	1.9817	2.1064±0.03	0.1247±0.0140	0.00569±0.00187

N: Coordination number

Reff： Reference Bond Length of FEFF calculation

R: Reff + ΔR

ΔR: Path Length Shift

σ² :Debye-Waller factor

Table S4. Specific activity (SA) values of M-SAE.

Samples	Km (μM)	Vmax (μM·min^{-1})	SA (U.mg^{-1})	[E](mol·L^{-1})	kcat (s^{-1})	kcat/Km （M^{-1}·S^{-1}）
Cu-SAE	324.57	0.00528	5.28 x10^{-5}	8.8188 x 10^{-5}	9.98 x10^{-7}	3.07 x 10^{-3}
Ag-SAE	56.497	0.00179	1.79 x10^{-5}	4.7252 x10^{-5}	6.31 x 10^{-7}	1.12 x 10^{-2}
Au-SAE	33.333	0.00138	1.38 x 10^{-5}	2.5974 x 10^{-5}	8.86 x 10^{-7}	2.66 x 10^{-2}